The International Journal of Advanced Manufacturing Technology (2019) 103:819–840
https://doi.org/10.1007/s00170-019-03580-x

ORIGINAL ARTICLE

# Experimental and simulation studies of abrasive particles impacting monocrystalline silicon in suspension thin film flow field of ultrasonic polishing

Tianqi Zhang [1,2] · Tianbiao Yu [1,2] · Tao Yang [1,2] · Zixuan Wang [1,2] · Ji Zhao [1,2]

Received: 5 November 2018 / Accepted: 11 March 2019 / Published online: 26 March 2019


## Abstract

In ultrasonic polishing (USP), when the gap between the polishing tool and workpiece is small enough, the suspension seeped into it can be considered as suspension thin film (STF). STF flow field provides a periodic oscillation condition for abrasive particles, which can improve abrasive particle cutting performance by changing its behavior. It is very effective for improving the polishing efficiency and surface quality of hard-to-machine materials. However, the interaction behavior of target material, STF flow field, and abrasive particle in USP has rarely been studied. In this paper, to fulfill a fundamental understanding of this field, the behavior of abrasive particles impacting monocrystalline silicon in STF flow field is investigated by experimental and simulation methods. At macro-level, through the study of ultrasonic amplitude, abrasive particle size, and polishing tool rotational speed in USP experiments, the positive role of STF flow field has been revealed, and the change characteristic of surface roughness is obtained. The computational fluid dynamics (CFD) simulation results show that strong transverse shear flow is formed in STF, which plays a major role in material removal. At micro-level, novel mathematical models of plastic deformation and brittleness removal and material removal mechanism of STF flow field are proposed. Comprehensive analysis of blunt and sharp abrasive particles impacting monocrystalline silicon is implemented through finite element method (FEM), which includes the effect of abrasive particle size on material removal rate (MRR), kinetic energy change of abrasive particle, force analysis of impact, the effect of impact angle, and polishing tool rotation on MRR. The final results show FEM simulation results are consistent with that of CFD simulation and experiments, which is of great significance to reveal the behavior principle of abrasive particles in STF and guide the actual production.

**Keywords** Ultrasonic polishing · Suspension thin film flow field · Abrasive particle behavior · CFD · FEM · Monocrystalline silicon

✉ Tianbiao Yu
tianbiaoyudyx@gmail.com; tbyu@mail.neu.edu.cn

Tianqi Zhang
tqz0120@126.com

Tao Yang
yt_shandong1990@163.com

Zixuan Wang
wangzixuan.neu@gmail.com

Ji Zhao
jzhao@mail.neu.edu.cn

[1] School of Mechanical Engineering and Automation, Northeastern University, Shenyang 110819, People's Republic of China

[2] Liaoning Provincial Key Laboratory of High-end Equipment Intelligent Design and Manufacturing Technology, Northeastern University, Shenyang 110819, People's Republic of China

## Nomenclature

| | |
|---|---|
| CAD | Computer-aided design |
| CFD | Computational fluid dynamics |
| CNC | Computer numerical control |
| CVD | Chemical vapor deposition |
| FEM | Finite element method |
| MRR | Material removal rate |
| NA | Numerical aperture |
| ROAP | Regular octahedron abrasive particle |
| SAP | Spherical abrasive particle |
| STF | Suspension thin film |
| U A - AWJP | Ultrasonic-assisted abrasive waterjet polishing |
| USP | Ultrasonic polishing |
| $A$ | Vibration amplitude of ultrasonic generator I |
| $a$ | Length of ROAP |

| | |
|---|---|
| $C$ | Dimensionless coefficient related to the crack form |
| $d$ | Abrasive particle size |
| $E$ | Elastic modulus of target material |
| $F$ | Reactive force by target surface (see Fig. 28 i) |
| $f_1$ | Non-dimensional coefficient |
| $f_2$ | Non-dimensional coefficient |
| $f_{\mathrm{I}}$ | Vibration frequency of ultrasonic generator I |
| $f_{\mathrm{II}}$ | Vibration frequency of ultrasonic generator II |
| $H$ | STF thickness (see Fig. 9) |
| $H_{\mathrm{m}}$ | Hardness of target material |
| $h$ | Depth pressed into target material (see Fig. 15) |
| $h_0^{\mathrm{roap}}$ | Actual depth of ROAP pressed into target material |
| $h_0^{\mathrm{sap}}$ | Actual depth of SAP pressed into target material |
| $I$ | Torque (see Fig. 28 i) |
| $K_{\mathrm{IC}}$ | Fracture toughness of target material |
| $l$ | Movement distance of abrasive particle |
| $m$ | Mass of abrasive particle |
| $m_{\mathrm{roap}}$ | Mass of ROAP |
| $m_{\mathrm{sap}}$ | Mass of SAP |
| $n$ | Polishing tool rotational speed |
| $Q$ | Volume change rate |
| $R$ | Radius of SAP |
| $S$ | Contact area of abrasive particle and target material |
| $S_d$ | Area of surface $a'b'c'd'$ |
| $S_{\mathrm{roap}}$ | Contact area of ROAP and target material |
| $S_{\mathrm{sap}}$ | Contact area of SAP and target material |
| $S_u$ | Area of surface $abcd$ |
| $T$ | Vibration period of ultrasonic generator I |
| $U_{\mathrm{C}}$ | Critical brittle fracture erosion kinetic energy of target material |
| $U_{\mathrm{D}}$ | Actual kinetic energy of impacting target material |
| $V$ | Material removal volume of single abrasive particle |
| $V_{\mathrm{roap}}$ | Volume of ROAP pressed into target material |
| $V_{\mathrm{sap}}$ | Volume of SAP pressed into target material |
| $V_{\mathrm{s}}$ | Volume of the suspension passing through cross section |
| $v$ | Velocity of abrasive particle |
| $v_1$ | Velocity of transverse shear flow (see Fig. 33) |
| $v_2$ | Velocity increment (see Fig. 33) |
| $v_{\mathrm{l}}$ | Linear velocity obtained by abrasive particle |
| $v_{\mathrm{pt}}$ | Velocity of polishing tool |
| $v_x$ | Flow velocity of $P$ in one vibration period |
| $v_{x1}$ | Flow velocity of $P$ in first half vibration period |
| $v_{x2}$ | Flow velocity of $P$ in second half vibration period |
| $z$ | Displacement of polishing tool |
| $\omega$ | Angular frequency of ultrasonic generator I |
| $\sigma_s$ | Approximate yield limit |
| $\rho$ | Density of abrasive particle |
| $\lambda$ | Influence coefficient of fluid resistance on velocity |
| $\xi$ | Efficiency of kinetic energy during impact |
| $\alpha$ | Radius angle (see Fig. 18) |
| $\theta$ | Impact angle (see Fig. 19) |

## 1 Introduction

Today is an era of unprecedented technological development. On the premise of meeting basic needs, the superior quality of products is becoming an essential problem. As a result, more and more advanced manufacturing methods have emerged, such as ultrasonic vibration–based, mechanical energy–based, thermal-based and electro-chemical-based. They can be used to process hard-to-machine and advanced materials (monocrystalline silicon, advanced ceramics, composites, etc.) with superior [1, 2]. Among these various available machining methods, ultrasonic machining is quite capable to process hard and brittle materials irrespective of their electrical and chemical properties, which are generally limitations for other techniques [3]. It thus is applied to various processes such as ultrasonic milling, ultrasonic grinding, ultrasonic drilling, and ultrasonic polishing (USP) [4–7]. Furthermore, excellent surface quality and mirror finish can only be obtained by polishing; however, polishing is very time-consuming; some scholars have tried to replace traditional polishing by improving grinding conditions and combined multiangle ultrasonic vibration with grinding [8, 9]. But grinding still has its limitations; therefore, it is of great significance to further investigate USP to improve its performance [10].

For better implementation of polishing, many scholars have made great efforts. Ralchenko et al. reported a fast polishing method of polycrystalline CVD diamond films based on ultrasonic machining in diamond slurry. Results showed that the developed method has a higher polishing rate than those known for mechanical or thermos-mechanical polishing and the surface roughness was reduced from Ra ≈ 5 to Ra ≈ 0.5 μm for the processing time as short as 5 min [11]. Hocheng et al. developed an innovative cost-effective USP system. Through polishing the entire surface in a patterned path, they observed micro-cutting, plowing, and indentation by abrasive on the polished surface and studied the effects of the abrasive size and static load on surface finish. They came to the conclusion that large static loads possess an advantage in that the abrasives are more effectively activated for polishing [12]. Kobayashi et al. presented a novel polishing apparatus and method for more effectively performing the edge polishing. They believed abrasive particles within the slurry held by the pad impact the work surface at an extremely high acceleration because of an elliptic ultrasonic vibration of the polishing pad which leads to high MRR [7]. Suzuki et al. proposed and developed an ultrasonic two-axis vibration–assisted polishing machine with piezo-electric actuators to

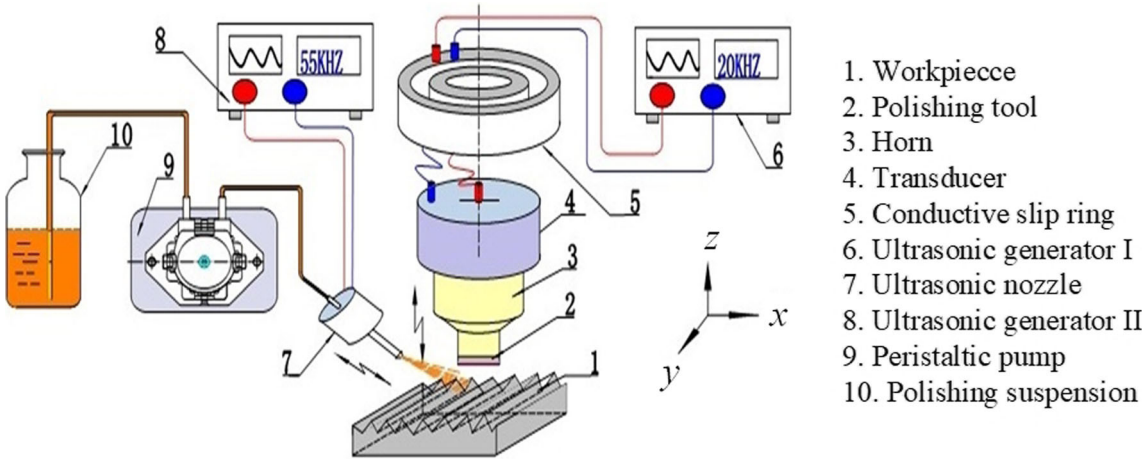


**Fig. 1** Experimental principle of USP

finish the micro-aspheric ceramic molds of high NA. The surface roughness of 8 nm Rz was obtained finally [13].

However, the studies available so far are mostly based on experiments and the effect of process parameters on MRR and polishing quality, while the behavior of suspension flow field and the performance of abrasive particle under the action of ultrasonic vibration have been rarely studied. Furthermore, the behavior of suspension flow field determines the performance of abrasive particles, and material removal mainly relies on abrasive particles [14]. Especially in USP, suspension flow field is greatly affected by high-frequency ultrasonic vibration. Therefore, the study should be laid stress on suspension flow field and its effect on abrasive particles. However, the solution to this problem is experimentally unavailable; as a supplement to experimental and theoretical work, computational fluid dynamics (CFD) and finite element method (FEM) are adopted in this study which provide an economically effective method to simulate real flows and impacting process for theoretical advances [15–18]. Such simulation methods are widely used in this kind of problem. Lv et al. simulated the fluid field of the impinging jet on the workpiece surface in ultrasonic-assisted abrasive waterjet polishing (UA-AWJP) and investigated the effects of workpiece vibration on pressure and velocity field of the impinging jet fluid field based on CFD. Finally, the measured experimental data was in reasonable agreement with simulation results [19]. Liu et al. established CFD models for ultrasonic velocity waterjets and abrasive waterjets using the Fluent6 flow solver. The results indicated that a jet is characterized by an initial rapid decay of the axial velocity at the jet center while the cross-sectional flow evolves toward a top-hat profile downstream [20]. Woytowitz simulated the impact of multiple spherical particles with a 3D FEM model and predicted the erosion rates by computing average damage and extrapolating to the level of 1.0. The results were in good agreement with the published experimental results [21]. ElTobgy et al. presented an elasto-plastic finite element model to simulate the erosion process in 3D configuration. The model took into account numerical and material damping, thermal elastic-plastic material behavior, and the effect of multiple particle impacts as well as material removal. The results were in agreement with published results obtained experimentally and from analytical erosion models [22].

In this paper, through experiments and the supports of CFD and FEM simulations, the interaction behavior among the

**Table 1** Experimental conditions of USP

| Parameters | Values |
|---|---|
| Polishing tool dimension | Diameter = 28 mm |
| Workpiece material | Monocrystalline silicon |
| Workpiece size | Length = 50 mm, width = 50 mm, height = 6 mm |
| Peristaltic pump flow range | 20 ml/min |
| Polishing suspension | Diamond suspension (3 wt%) |
| Abrasive particle size ($d$) | 1.5 μm, 2.5 μm, 3.5 μm |
| Polishing tool rotational speed ($n$) | 0 rpm, 360 rpm, 480 rpm, 600 rpm |
| Vibration frequency of ultrasonic generator I ($f_{\mathrm{I}}$) | 20 kHz |
| Vibration amplitude of ultrasonic generator I ($A$) | 0 μm, 9 μm, 15 μm, 21 μm |
| Vibration frequency of ultrasonic generator II ($f_{\mathrm{II}}$) | 55 kHz |
| STF thickness ($H$) | 100 μm |

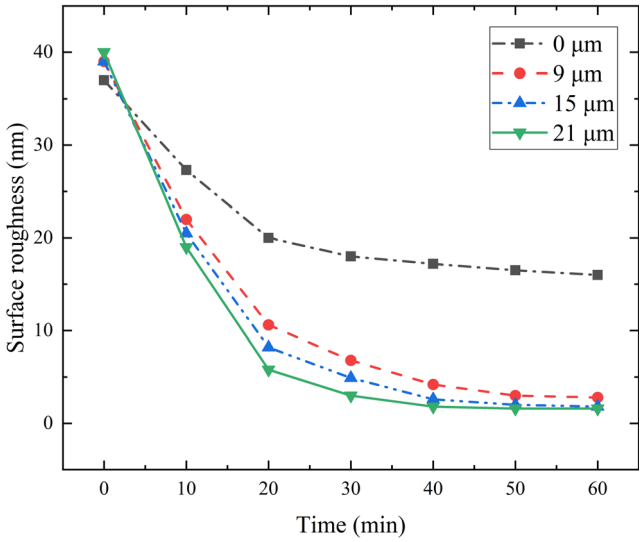


**Fig. 2** Time curves of surface roughness with different ultrasonic amplitudes

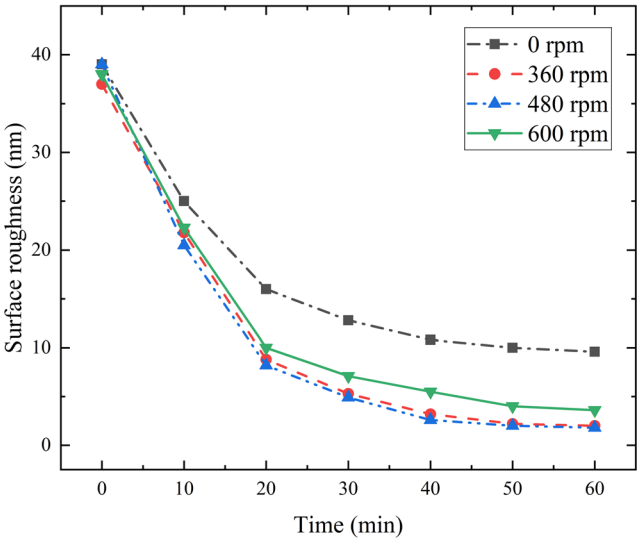


**Fig. 4** Time curves of surface roughness with different polishing tool rotational speeds

material, suspension thin film (STF) flow field, and abrasive particle under USP can be established, thereby the behavior of abrasive particles impacting monocrystalline silicon in STF flow field is investigated to fulfill a fundamental understanding of this field

## 2 Experimental setup of USP

### 2.1 Experimental principle

The experiments are performed on a self-refitted 3-axis CNC milling machine, and the details can be found in [23, 24]. It provides axial ultrasonic vibration for the polishing tool by ultrasonic generator I, which has a vibration frequency of 20 kHz and an amplitude range from 0 to 32 μm. Ultrasonic generator II with a vibration frequency of 55 kHz and constant amplitude is equipped to provide high-frequency ultrasonic vibration for polishing suspension nozzle, which can make the suspension atomized and sprayed evenly. Polishing suspension is supplied by peristaltic pump. The workpiece is fixed on the machine table with bonding glue. During the polishing process, the gap between the polishing tool and workpiece surface is kept within a fixed range. In recent years, ultrasonic devices have been gradually applied to an ultra-precision machine tool; meanwhile, automation and intelligence of USP have been gradually realized. Therefore, accurate positioning makes the gap between the polishing tool and workpiece surface be greatly reduced. Because the gap size is small enough and the suspension flow space is limited to this gap, the suspension flow field is considered as STF flow field. Under the joint effect of the two ultrasonic vibrations and the STF flow field, the performance of abrasive particles has been greatly improved. The experimental principle of USP is shown in Fig. 1.

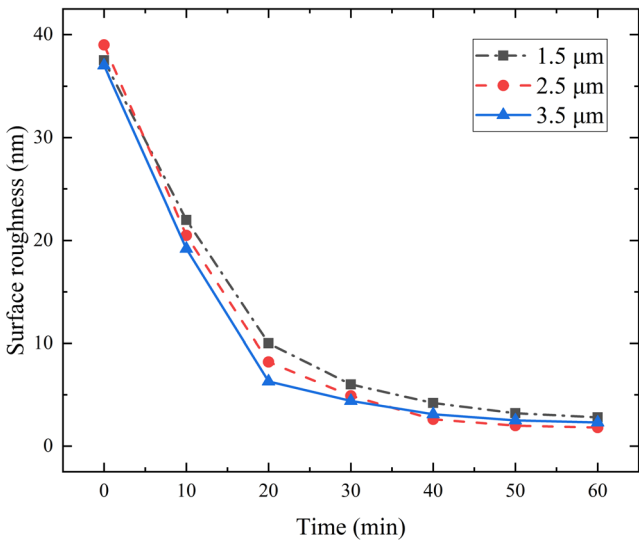


**Fig. 3** Time curves of surface roughness with different abrasive particle sizes

### 2.2 Experimental conditions

Before USP, the monocrystalline silicon workpieces were hand polished with abrasive papers. The conditions are listed in Table 1.

## 3 Experimental results and discussions

The generated surfaces are measured correspondingly by 3D measuring laser microscope. Five points of each group are measured; in addition to the measured maximum and minimum, the remaining three points are selected for

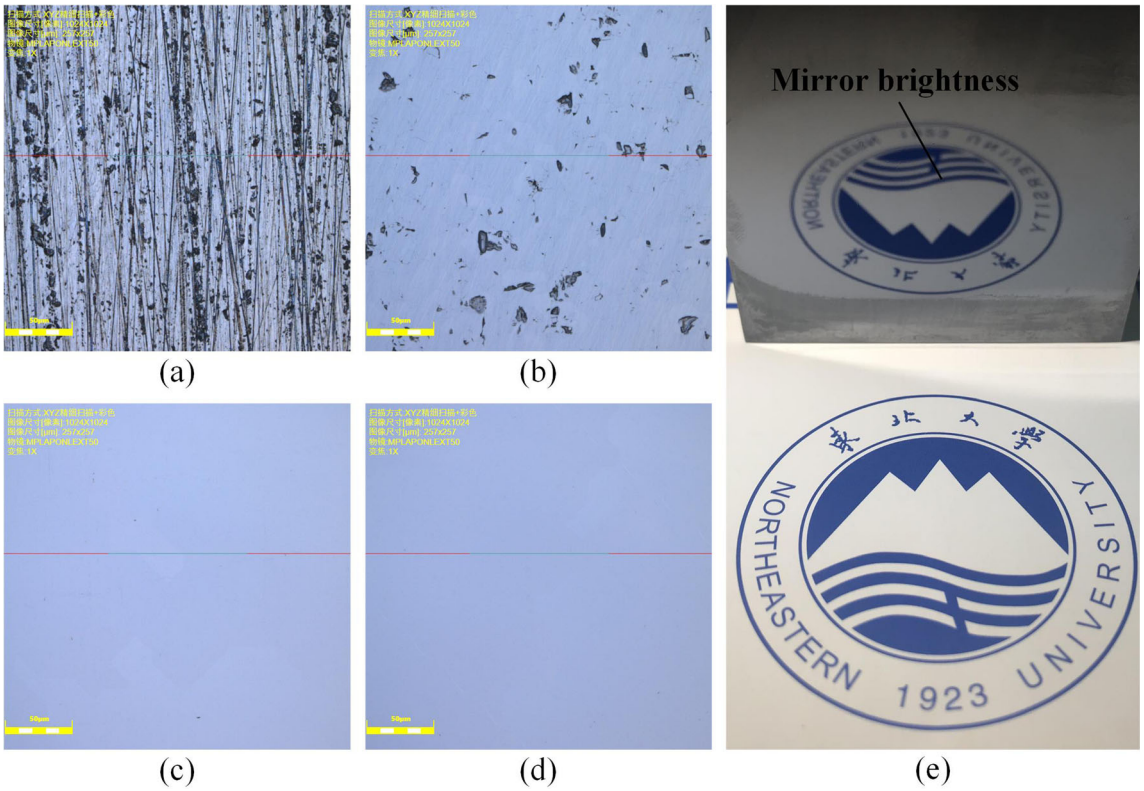


**Fig. 5** Quality comparison of polishing at each stage under certain polishing parameters

avoiding contingency. The average of selected points is taken as the final roughness value.

### 3.1 Effects of vibration amplitude of ultrasonic generator I on surface quality

When $d$ is 2.5 μm, $n$ is 480 rpm, and $A$ values are 0 μm, 9 μm, 15 μm, and 21 μm respectively, the time curves of surface roughness are shown in Fig. 2. The surface roughness decreases rapidly in the first 20 min. As the polishing time approaches 60 min, surface roughness tends to be stable. Within the same polishing time, a better surface quality can be generated through USP than general polishing ($A = 0$ μm). Especially in the first 20 min, the larger the amplitude is, the faster the surface roughness decreases. As the amplitude increases gradually from 9 μm to 15 μm and 21 μm, the final surface roughness becomes lower and lower. It is worth noting that after polishing for about 50 min, the surface roughness of 15 μm and 21 μm is very close to each other which means the increasing amplitude properly is beneficial to improving the surface quality.

### 3.2 Effects of abrasive particle size on surface quality

When $n$ is 480 rpm, $A$ is 15 μm, $d$ values are 1.5 μm, 2.5 μm, and 3.5 μm respectively, the time curves of surface roughness are shown in Fig. 3. In the first 20 min, the curve of 3.5 μm changes the most obviously, followed by the curve of 2.5 μm, and that of 1.5 μm changes the most gradually which indicates that abrasive particle size affects the polishing efficiency. According to the average roughness, the surface quality of 2.5 μm is better than that of 3.5 μm, and that of 1.5 μm still has a downward trend after polishing for 60 min, which indicates that the increase of abrasive particle size has adverse effects on the surface quality; nonetheless, large abrasive particles are suitable for rough polishing.

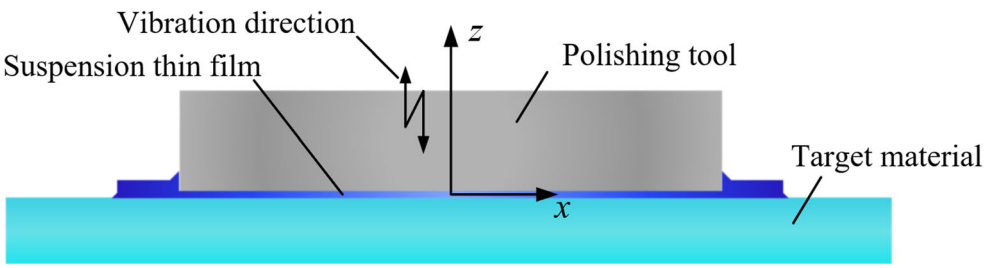


**Fig. 6** Schematic diagram of USP model

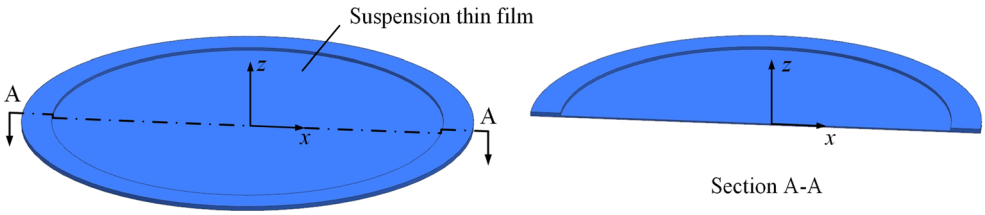


**Fig. 7** Shape of STF

### 3.3 Effects of polishing tool rotational speed on surface roughness

When $d$ is 2.5 μm, $A$ is 15 μm, $n$ values are 0 rpm, 360 rpm, 480 rpm, and 600 rpm respectively, the time curves of surface roughness are shown in Fig. 4. In the first 20 min, the roughness curve of 480 rpm changes most obviously, followed by the curves of 360 rpm and 600 rpm and the curve of 0 rpm changes the most gradual. It indicates that polishing tool rotation is of great significance, and as $n$ increases, the improvement of polishing efficiency belongs to the trend of first increase and then decrease. This is because when $n$ increases from 360 to 480 rpm, the increased rotational speed promotes the even distribution of abrasive particles, which is beneficial to improve the polishing efficiency. When $n$ increases to 600 rpm, as the rotating speed increases, the centrifugal force of polishing tool increases and abrasive particles are difficult to soak into the gap between polishing tool and workpiece, which, instead, leads to a decrease in polishing efficiency.

### 3.4 Surface morphology at each polishing stage under certain polishing parameters

When $A$ is 15 μm, $n$ is 480 rpm, and $d$ is 2.5 μm, the surface morphologies under a laser microscope at each stage are shown in Fig. 5; (a) after hand polished with abrasive paper (Ra = 39 nm), there are sharp scratches; (b) after USP for 20 min (Ra = 8.2 nm), scratches are greatly reduced, but a few depressions are still visible; (c) after USP for 40 min (Ra = 2.6 nm), surface becomes very smooth, and depressions have disappeared; (d) after polishing for 60 min (Ra = 1.8 nm), there is no obvious change in the surface compared with (c); (e) mirror brightness is obtained after polishing for 60 min.

According to the changes in surface roughness at each stage, the material removal rate decreases with polishing time. Until polishing reaches a certain time, there is no significant difference in surface roughness under laser microscope.

## 4 Simulated analysis of STF flow field

According to the above experimental results, ultrasonic vibration indeed has a positive effect on polishing. The reasons for this effect have been briefly analyzed through experiments at micro-level; nevertheless, the immanent cause is still unclear.

In polishing process, material removal mainly depends on abrasive particles, and their behavior acting on target material surface is the direct cause resulting in the material removal [25, 26]. In USP, STF flow field provides a different condition for abrasive particles and its characteristics determine a different behavior of abrasive particles [27]. Understanding the abrasive particles characteristics during USP is a prerequisite to further reveal the material removal mechanism of monocrystalline silicon. Therefore, in order to further analyze the correlation between ultrasonic vibration parameters and abrasive particle behavior as well as the surface quality, and apply USP in the future, the characteristics of STF flow field should be studied concretely.

### 4.1 Modeling of STF flow field

To make a comprehensive analysis of STF flow field for USP, CFD simulation is adopted. The formed STF between

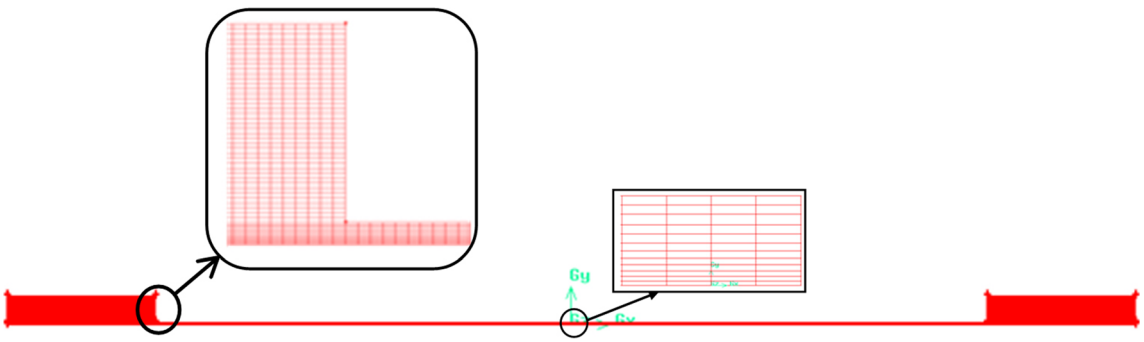


**Fig. 8** Two-dimensional grid diagram of STF flow field

**Table 2** Boundary setting of the calculation model

| Boundary | Length (mm) | Property | Type |
|---|---|---|---|
| AB | 5 | Outlet | Pressure-outlet |
| BC | 3 | Deforming | wall |
| CD | 10 | Moving wall | wall |
| DE | 3 | Deforming | wall |
| EF | 5 | Outlet | Pressure-outlet |
| FG | 5 | Wall | wall |
| GH | 30 | Wall | wall |

polishing tool and target surface is shown in Fig. 6 and its shape can be described as shown in Fig. 7.

In CFD simulation, the characteristics of STF flow field are studied by changing vibration amplitude (9 μm, 15 μm, 21 μm) and STF thickness (80 μm, 100 μm, 120 μm). The diameter of the polishing tool is set for 28 mm. In order to fully reflect the characters of STF, it needs not only to ensure the grid of simulation model no less than 10 layers but also to refine the grid at the wall for more accurately reflecting the fluid velocity. On account of the axisymmetric structure of the established model and its circumferential dimension being much larger than the axial dimension which meets the conditions of FLUENT for establishing a two-dimensional model, two-dimensional flow field simulation model is established for simplifying calculation. The grid of the model is divided in GAMBIT software as shown in Fig. 8.

The model boundary conditions are set as shown in Table 2. The model length is shown in Fig. 9 (L1 = L2 = 5 mm, L3 = L5 = 1 mm, L4 = 38 mm); *H* is the STF thickness.

## 4.2 Simulation model—pressure and velocity analysis of STF flow field

The pressure and velocity of STF flow field model are analyzed. The parameters are set as $A = 15$ μm and $H = 100$ μm. $T$ is the vibration period of ultrasonic generator I. Four time points ($T/4$, $T/2$, $3T/4$, and $T$) are selected to analyze pressure change. Pressure values on the wall of four time points are shown in Fig. 10. The pressure of the whole STF flow field is constantly changing from positive to negative. The maximum pressure is about $3 \times 10^8$Pa. Compared with the maximum pressure $2 \times 10^6$Pa of the 2-mm thickness we simulated, the pressure of STF model changes more violently.

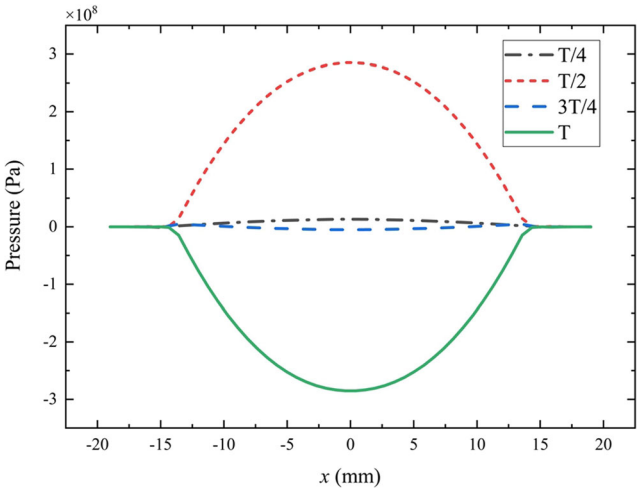


**Fig. 10** Pressure change curves of STF flow field on target material surface

Velocity curves of STF flow field at four time points in $x$ direction are shown in Fig. 11. It can be seen that velocity in $x$ direction is bilaterally symmetrical and increases as moving away from the origin of the coordinates. Compared with the 2-mm thickness film of maximum velocity 2.3 m/s we simulated, the horizontal velocity of the 100-μm thickness STF increases to a maximum velocity of about 70 m/s.

Velocity curves of STF flow field at four time points in $z$ direction are shown in Fig. 12. The velocity in $z$ direction at target material surface, which is directly below polishing tool, increases as moving away from the origin of the coordinates. The velocity difference of four time points is not evident. Compared with 2-mm thickness film of maximum longitudinal velocity 0.15 m/s we simulated, that of the 100-μm thickness STF is about 0.2 m/s. There is no evident change. However, the velocity in $z$ direction at the edge of polishing tool could reach a velocity value of 2–3 m/s. This is because the flow field here has convection with that in outer space; suspension is more active and makes the velocity here skyrocket.

All of the above prove both pressure and velocity in STF flow field change periodically, which cause the periodic fluctuation of suspension. Under such conditions, the behavior of abrasive particles is greatly affected. In addition to improving the MRR of abrasive particles, their irregularity degree of impacting also has been increased, which are both beneficial to improve polishing performance. Moreover, it can be seen

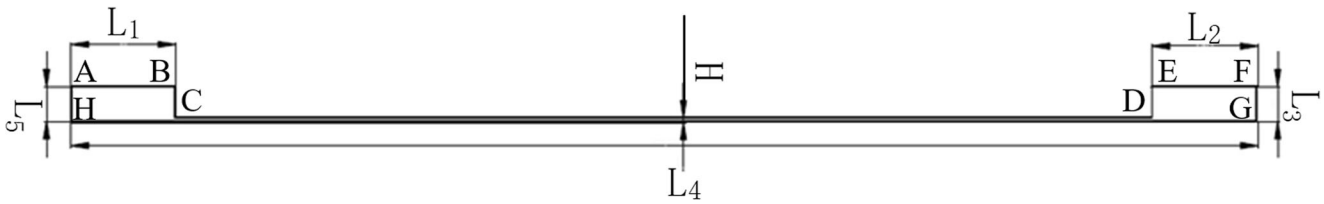


**Fig. 9** Two-dimensional diagram of the simulation model

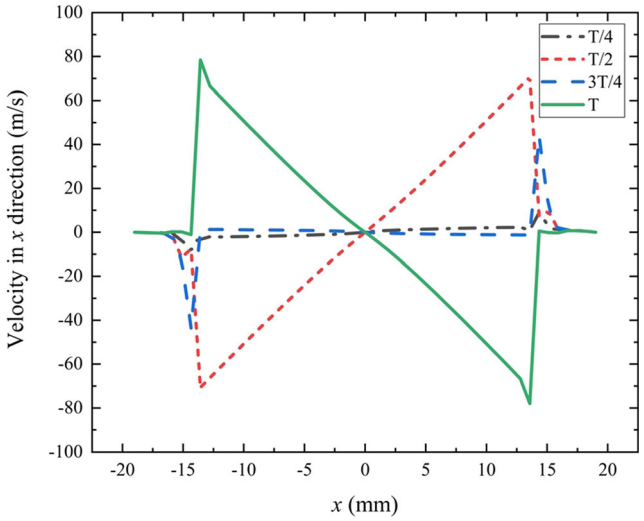


**Fig. 11** Velocity curves in $x$ direction

from the comparative analysis above that the reduction of $H$ from 2 mm to 100 μm does not make the maximum velocity in vibration direction ($z$ direction) increase obviously; it only increases from 0.15 to 0.2 m/s, and the maximum transverse velocity increased significantly from 2.3 to 70 m/s. Therefore, conclusions can be drawn that strong transverse shear flow generates in STF, which has a large contribution to material removal in USP.

### 4.3 Simulation model—the effect of amplitude on velocity of STF flow field

$H$ is set to 100 μm, and the $A$ values are 9 μm, 15 μm, and 21 μm respectively. Under the given sinusoidal velocity inlet condition, the velocity curves in the $x$ direction at the wall surface corresponding to the three amplitudes at $T/2$ are shown in Fig. 13.

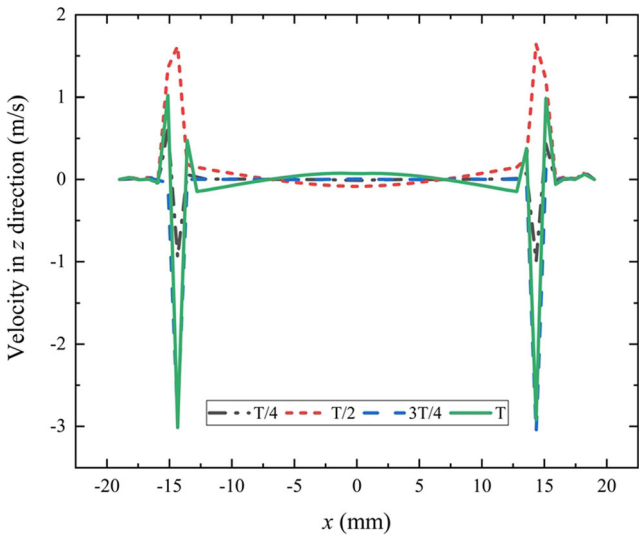


**Fig. 12** Velocity curves in $z$ direction

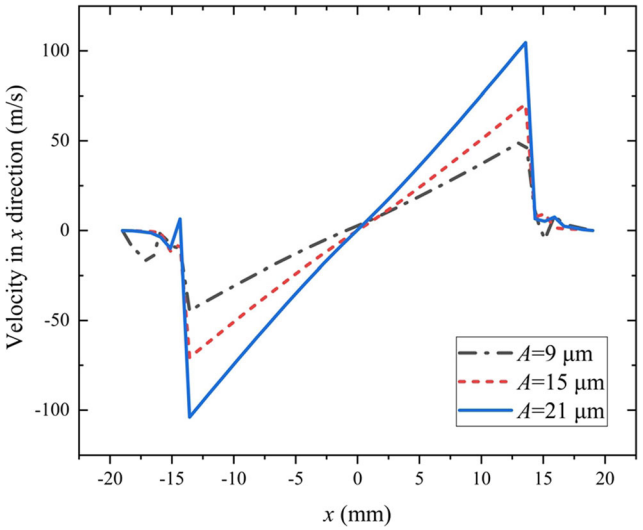


**Fig. 13** Velocity curves in $x$ direction

According to the motion equation of the dynamic mesh, the velocity equation increases with the increase of amplitude. As shown in Fig. 13, the velocity in $x$ direction increases as the amplitude increases. For the velocities in $x$ direction of the wall surface, the maximum velocities corresponding to the amplitude of 9 μm, 15 μm, and 21 μm are 51 m/s, 70 m/s, and 104 m/s respectively, which means under the condition of STF flow field, the increase of ultrasonic amplitude will promote the increase of transverse shear flow velocity.

### 4.4 Simulation model—effect of STF thickness on velocity of STF flow field

$A$ is set to 15 μm, and the $H$ values are 80 μm, 100 μm, and 120 μm respectively. Under the given sinusoidal velocity inlet condition, the velocity curves in $x$ direction

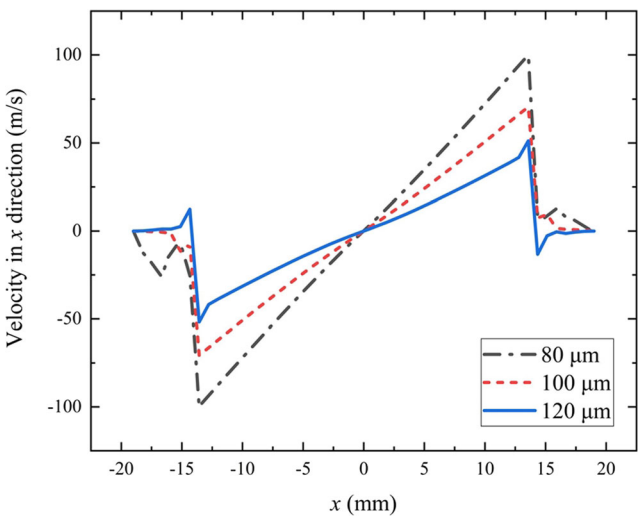


**Fig. 14** Velocity curves in $x$ direction

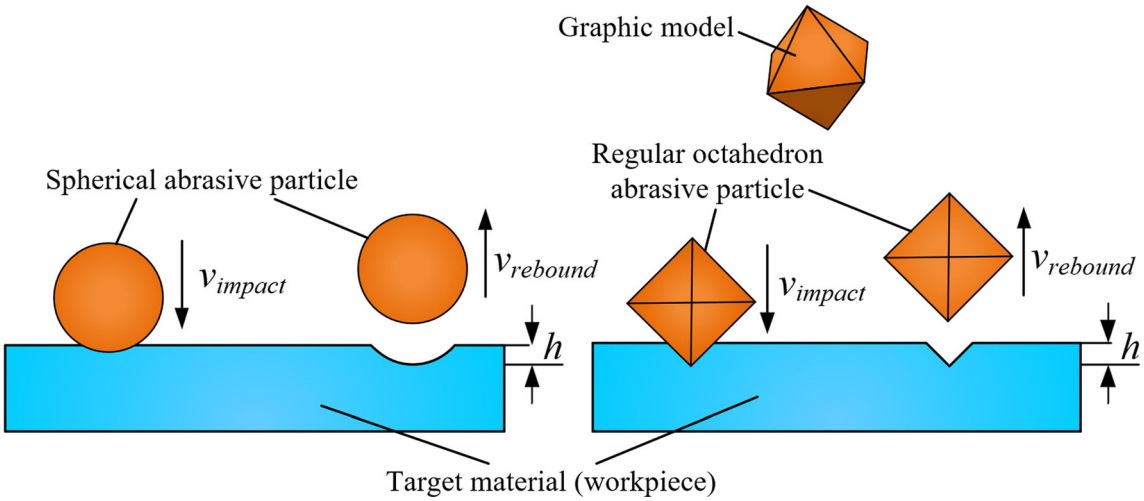


**Fig. 15** Schematic of plastic deformation stage

at the wall surface corresponding to the three thicknesses at $T/2$ are shown in Fig. 14.

As shown in Fig. 14, the velocity in $x$ direction increases as the STF thickness decreases. For the velocity in $x$ direction of the wall surface, the maximum velocities corresponding to the thickness of 80 μm, 100 μm, and 120 μm are 101 m/s, 70 m/s, and 50 m/s respectively. Therefore, reducing the STF thickness can increase the transverse shear flow.

## 5 Simulated analysis of abrasive particles impacting monocrystalline silicon

The formation essence of transverse shear flow in STF is the ultrasonic vibration of polishing tool. When the initial phase of ultrasonic vibration is not considered, displacement equation of polishing tool can be described as

$$z = A\sin(\omega t) \tag{1}$$

where $\omega = 2\pi f_I$, which is the angular frequency of ultrasonic generator I. The velocity equation of polishing tool thus can be given by

$$v_{pt} = \frac{dz}{dt} = \omega A\cos(\omega t) \tag{2}$$

### 5.1 Theoretical analysis of ultrasonic mechanics

Over the last few decades, many scholars have conducted a lot of indentation tests on various hard and brittle materials. It is concluded that even hard brittle materials may have plastic deformation characteristics similar to plastic materials under a low load [28–30]. Therefore, when the abrasive particles impact target material at low velocity, it will leave a small plastic deformation. Only when the velocity increases to a certain value and the impact depth of abrasive particle is greater than the maximum critical value of plastic compression, will the brittle crack and fracture generate on the target material surface [31]. In this study, a deep research is taken on mathematical model of USP mechanism. To simplify the

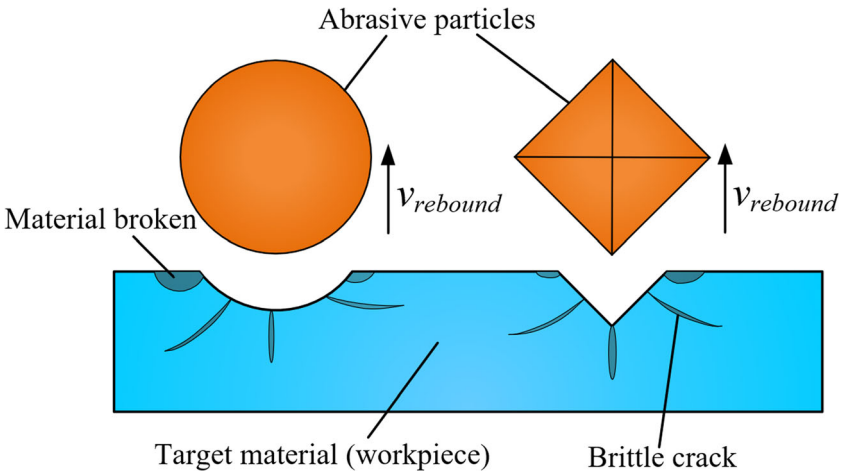


**Fig. 16** Schematic of brittleness removal stage

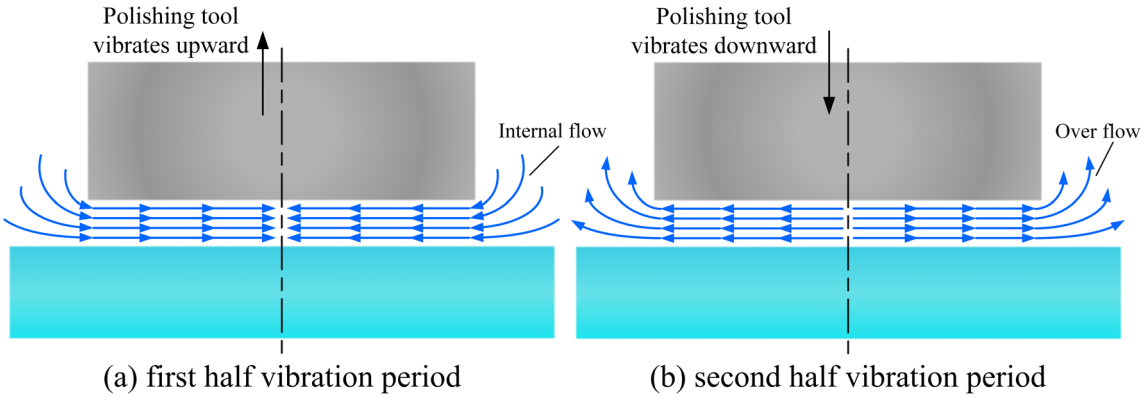


**Fig. 17** The STF schematic in one vibration period: **a** first half vibration period and **b** second half vibration period

calculation model, several assumptions are made as follows: (1) single abrasive particle impacts directly on the target material, there is no energy exchange with other abrasive particles, (2) the working fluid medium is uniformly distributed, (3) the abrasive particle incident direction is perpendicular to the tangent plane at the impact location on target material surface for theoretical analysis, (4) the fracture of workpiece surface caused by impact is ignored, (5) effects of cavitation and other effects on abrasive particles are ignored.

#### 5.1.1 Stage of plastic deformation

**Impact depth** When impact depth is greater than maximum elastic compression depth, plastic deformation occurs firstly on the target material surface [32, 33]. It means the deformation of material has exceeded the reversible elastic deformation and changed to irreversible plastic deformation as shown in Fig. 15. In this process, the stress does not increase much with the increase of strain and before tress reaches the approximate yield limit $\sigma_s$, plastic deformation, and contact area $S$ do not change much.

Abrasive particles in suspension are approximately considered as spherical and regular octahedron respectively. Spherical is used to simulate abrasive particles with a blunt surface profile while regular octahedron is used to simulate those with the sharp surface profile.

- Spherical abrasive particle (SAP). When SAP impacts target material and the volume pressed into material is less than half of the abrasive particle, the volume can be described as

$$V_{\text{sap}} = \frac{1}{3}\pi(3R-h) \times h^2 \tag{3}$$

The contact area of abrasive particle and the target material is

$$S_{\text{sap}} = 2\pi R{\cdot}h \tag{4}$$

where $R$ is the radius of SAP, and $h$ is the depth pressed into the target material. Compared with the radius $R$, the depth $h$ of each impact is very small; thus, formula (3) can be approximately rewritten as

$$V_{\text{sap}} = \pi R h^2 \tag{5}$$

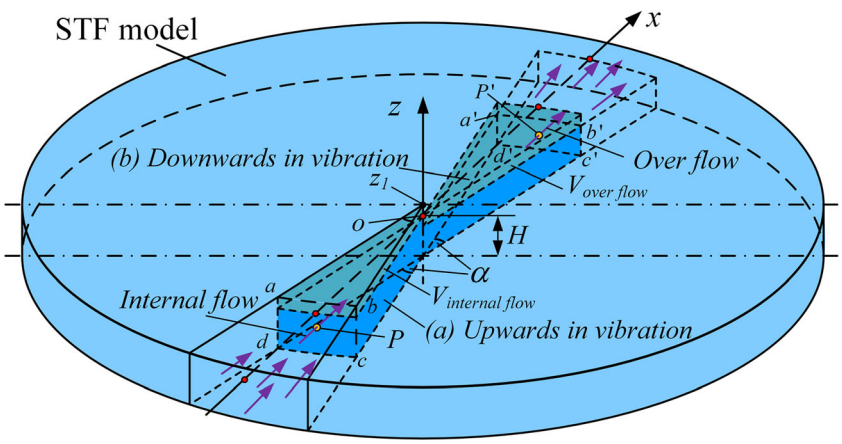


**Fig. 18** The schematic of internal flow and over flow

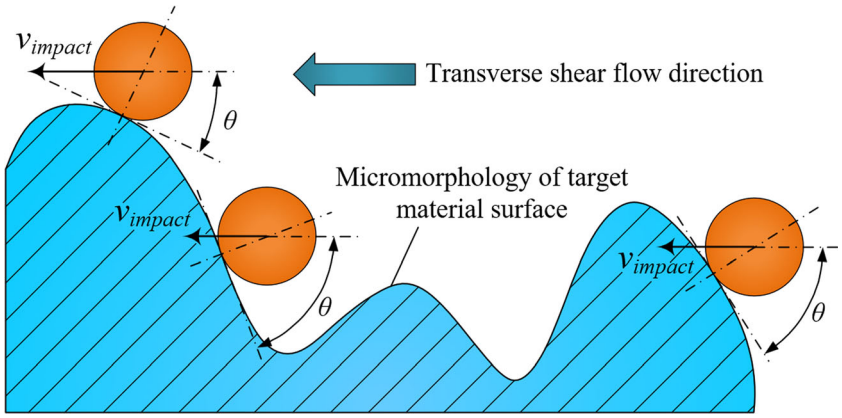


**Fig. 19** Schematic of abrasive particles impacting the target material surface

When yield stress is about $2\sigma_s$, plastic material begins to yield; the relation between impact depth and impact velocity can be obtained by

$$\frac{1}{2}m_{\text{sap}}v^2 = \int_0^{h_0} 2\sigma_s \times 2\pi R \times hdh \tag{6}$$

where $m_{\text{sap}}$ is the mass of SAP, and $v$ is the velocity of the abrasive particle. $m_{\text{sap}}$ can be obtained by

$$m_{\text{sap}} = \frac{4}{3}\pi R^3 \times \rho \tag{7}$$

where $\rho$ is the density of the abrasive particle. Combining formulas (6) and (7), the actual depth ${h_0}^{\text{sap}}$ can be calculated by

$${h_0}^{\text{sap}} = v\sqrt{\frac{\rho R^2}{3\sigma_s}} \tag{8}$$

- Regular octahedron abrasive particle (ROAP). Similarly, the volume of ROAP pressed into the target material is defined as

$$V_{\text{roap}} = \frac{2}{3}h^3 \tag{9}$$

The contact area of ROAP and target material is

$$S_{\text{roap}} = 2\sqrt{3}h^2 \tag{10}$$

Similarly, the relationship between impact depth and impact velocity can be obtained by

$$\frac{1}{2}m_{\text{roap}}v^2 = \int_0^{h_0} 2\sigma_s \times 2\sqrt{3}h^2 dh \tag{11}$$

Mass of ROAP is

$$m_{\text{roap}} = \frac{1}{3}\sqrt{2}a^3 \times \rho \tag{12}$$

where $a$ is the length of a regular octahedron. Thus

$${h_0}^{\text{roap}} = a\left(\frac{\sqrt{6}\rho v^2}{24\sigma_s}\right)^{1/3} \tag{13}$$

**Material removal volume of the single abrasive particle** Our previous studies have proved that ultrasonic vibration makes the abrasive particles obtain instantaneous acceleration and an initial velocity. However, the abrasives particles are immersed in suspension and impact the target material surface together with the suspension. In this process, the velocity will decay as the movement distance increases. Therefore, the velocity attenuation equation can be written as

$$v = \omega \times A \times \cos(\omega \times t) \times e^{-\lambda l} \tag{14}$$

where $\lambda$ is the influence coefficient of fluid resistance on velocity, and $l$ is the movement distance.

**Table 3** Performance parameters of diamond materials

| Material | Density (g/cm$^3$) | The Young modulus (GPa) | The Poisson ratio | The Vickers hardness (GPa) |
|---|---|---|---|---|
| Diamond | 3.515 | 1000 | 0.07 | 50 |

**Table 4** Performance parameters of monocrystalline silicon corresponding to JH-2

| Performance parameters | Values |
|---|---|
| Density | 2300 |
| Shear modulus (GPa) | 61.7 |
| A | 0.85 |
| B | 0.31 |
| C | 0.013 |
| M | 0.21 |
| N | 0.29 |
| EPSI | 1.0 |
| Tensile strength (GPa) | 260 |
| HEL (GPa) | 0 |
| PHEL (GPa) | 9 |
| HEL body strain rate | 5 |
| HEL intensity (GPa) | 1.0 |
| D1 | 0.02 |
| D2 | 1.85 |
| K1 (GPa) | 201 |
| K2 (GPa) | 260 |
| K3 (GPa) | 0 |
| Beta | 1.0 |

Substituting formula (14) into formula (8), the depth generated by SAP impacting into the target material can be obtained by

$$h_0{}^{\text{sap}} = \omega \times A \times \cos(\omega \times t) \times e^{-\lambda l}\sqrt{\frac{\rho R^2}{3\sigma_s}} \tag{15}$$

Therefore, according to formula (5), the deformed volume caused by single SAP can be expressed as

$$V_{\text{sap}} = \frac{\pi\rho R^3\omega^2A^2\cos^2(\omega \times t)e^{-2\lambda l}}{3\sigma_s} \tag{16}$$

Similarly, substituting formula (14) into formula (13), the depth generated by ROAP impacting into the target material can be obtained by

$$h_0{}^{\text{roap}} = a\left(\frac{\sqrt{6}\rho\omega^2A^2\cos^2(\omega \times t)e^{-2\lambda l}}{24\sigma_s}\right)^{1/3} \tag{17}$$

According to formula (9), the deformed volume caused by single ROAP during plastic deformation stage is

$$V_{\text{roap}} = \frac{\sqrt{6}\rho a^3\omega^2A^2\cos^2(\omega \times t)e^{-2\lambda l}}{36\sigma_s} \tag{18}$$

### 5.1.2 Stage of brittle removal

When the impact depth of abrasive particles is greater than the maximum plastic compression depth, brittle cracks occur. On this occasion, material removal is not limited to plastic deformation. The schematic of the brittle removal stage is shown in Fig. 16. The actual kinetic energy of the abrasive particle impacting target material is [34]

$$U_{\text{D}} = \frac{1}{2}\xi mv^2 \tag{19}$$

where $m$ is the mass of abrasive particle, and $\xi$ is the efficiency of kinetic energy during impact.

Substituting formula (14) into formula (19), the actual kinetic energy of the abrasive particle impacting the target material is expressed as

$$U_{\text{D}} = \frac{1}{2}\xi m\omega^2A^2\cos^2(\omega \times t)e^{-2\lambda l} \tag{20}$$

Removal mechanism is determined by comparing $U_{\text{D}}$ with critical brittle fracture erosion kinetic energy of target material $U_C$. $U_C$ is described as [34]

$$U_C = C\frac{E^{3/2}{K_{IC}}^6}{{H_m}^{13/2}} \tag{21}$$

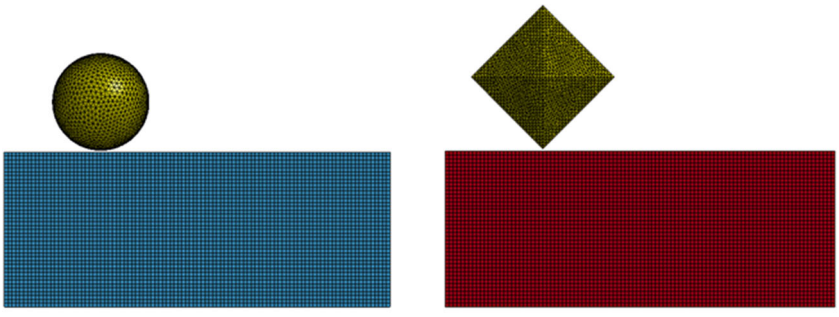

(a) SAP (b) ROAP

**Fig. 20** Simulation model after grid division: **a** SAP and **b** ROAP

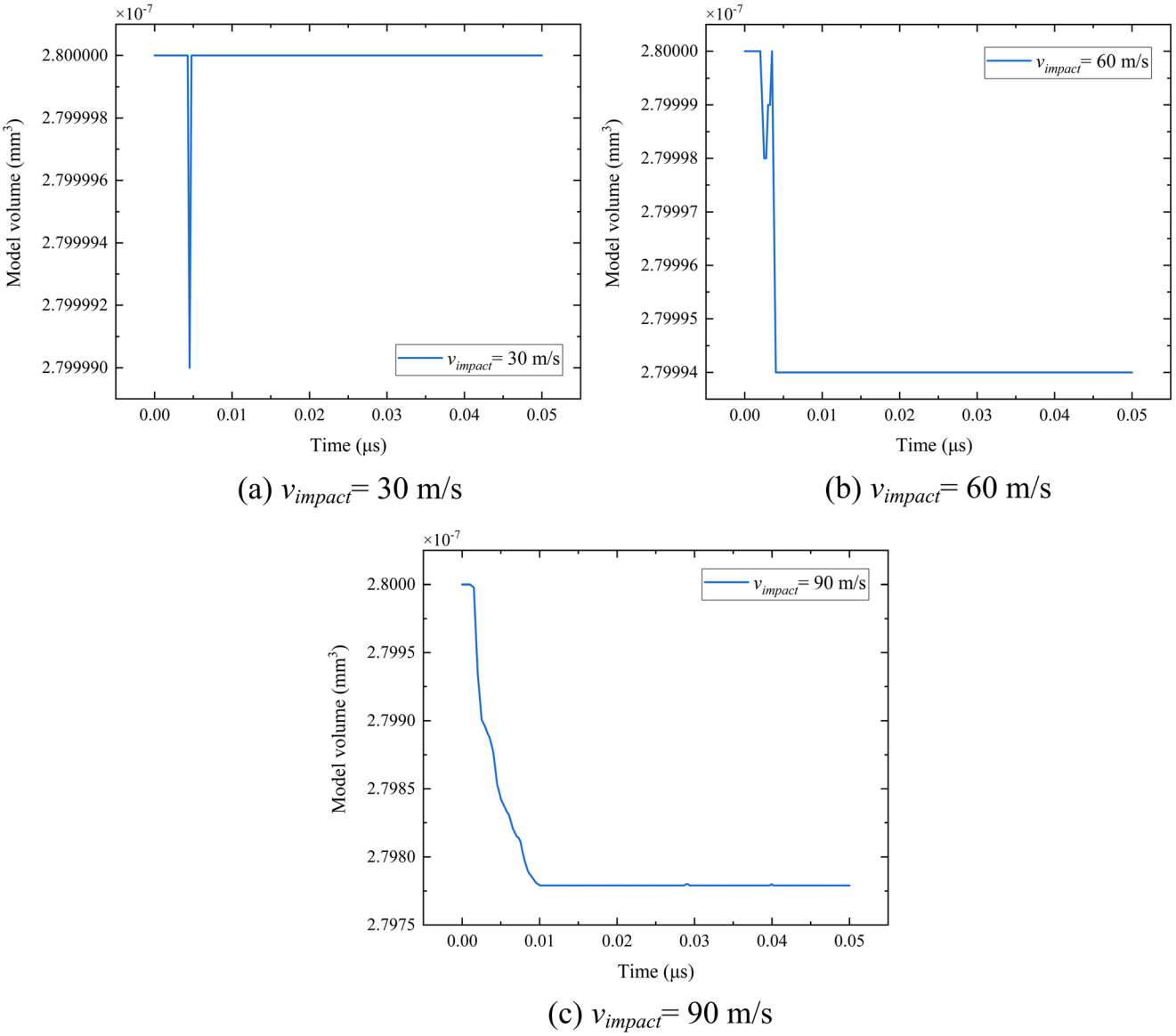


**Fig. 21** Volume curves when impact angel is 30°: **a** $v_{impact} = 30$ m/s, **b** $v_{impact} = 60$ m/s, and **c** $v_{impact} = 90$ m/s

where $C$ is the dimensionless coefficient related to the crack form, and $E(GPa)$, $H_m(GPa)$, and $K_{IC}(\mathrm{MPa} \times \mathrm{m}^{1/2})$ are the elastic modulus, hardness, and fracture toughness of target material respectively. If $U_D > U_C$, the main removal method of material is brittle removal. Material removal volume of single abrasive particle is

$$V = f_1 \frac{E^{5/4} {U_D}^{7/6}}{{H_m}^{17/12} K_{IC}} \left(1 - f_2 \frac{E^{1/4} K_{IC}}{{H_m}^{13/12} {U_D}^{1/6}}\right) \tag{22}$$

where $f_1$ and $f_2$ are non-dimensional coefficient reflecting the effect of factors such as material fracture mode and abrasive particle geometry on material removal mechanism.

According to the above analysis, despite the fact that the material removal method is plastic deformation or brittle removal, material removal is affected by ultrasonic vibration frequency $f$, ultrasonic amplitude $A$, abrasive particle geometry, material properties, and so on.

## 5.2 Simulation analysis of abrasive particles impacting monocrystalline silicon based on LS-DYNA

Abrasive particles impacting on target material surface involves situations such as collision, deformation, and fracture. According to CFD simulation results above, in USP, the horizontal velocity of the 100-μm thickness STF flow field increases to a maximum of about 70 m/s. Therefore, its contact time with the target material is extremely short. Moreover, the abrasive particles are very small. It is difficult to directly observe the impact process of abrasive particles through experiments. Therefore, many studies have been focused on the numerical simulation of abrasive particles impact process [35–38].

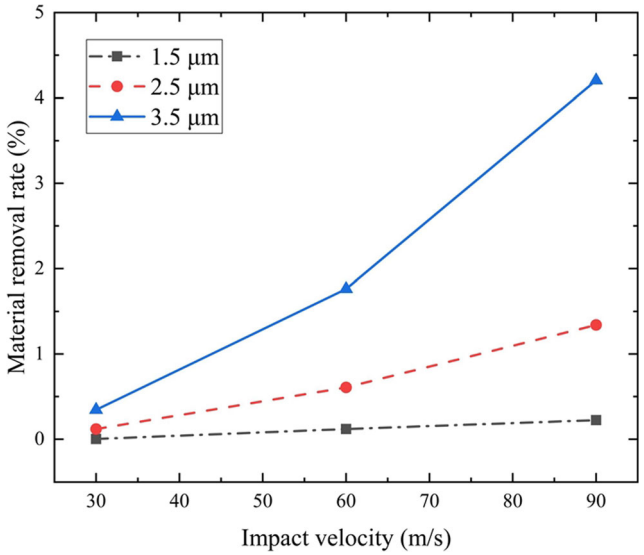


**Fig. 22** Relation curves between MRR and impact velocity

### 5.2.1 Material removal mechanism of abrasive particles impacting target material surface in STF of USP

According to pressure and velocity simulation analysis of STF flow above, the material removal mainly depends on transverse shear flow. That is because the gap between the polishing tool and target becomes large and small periodically due to the effect of ultrasonic vibration; meanwhile, the suspension within the gap generates internal flow and overflow periodically. As shown in Fig. 17 a, in the first half vibration period, polishing head vibrates along the direction away from the workpiece. In this process, the instant increase of the gap size results in the generation of suspension internal flow. The suspension outside the gap moves inwards to the center due to atmospheric pressure as shown in Fig. 18 a. $P$ is a point on the cylindrical surface $abcd$, when the polishing head vibrates to $z_1$ at time $t$. The volume of the suspension passing through the cylindrical surface $abcd$ is

$$V_s = \frac{1}{2}\alpha A\sin(2\pi f_1 t)x^2 \tag{23}$$

where $\alpha$ is the radius angle shown in Fig. 18. Therefore, the volume change rate $Q$ can be obtained by taking the derivative of formula (23) with respect to $t$

$$Q = \pi f_1 \alpha A\cos(2\pi f_1 t)x^2 \tag{24}$$

When $\alpha$ is infinitely close to zero, the flow velocity of $P$ in first half vibration period is

$$v_{x_1} = \frac{Q}{S_u} = -\frac{\pi f_1 A\cos(2\pi f_1 t)}{H + A\sin(2\pi f_1 t)}x \tag{25}$$

where $S_u$ is the area of the surface $abcd$.

In the second half vibration period, polishing tool vibrates toward workpiece as shown in Fig. 17 b. But its principle is in reverse of the first half period as shown in Fig. 18 b; the over the flow of suspension generates in this process. According to the same principle as the first half period, the flow velocity of $P$ in the second half period is

$$v_{x_2} = \frac{Q}{S_d} = -\frac{\pi f_1 A\cos(2\pi f_1 t)}{H - A\sin(2\pi f_1 t)}x \tag{26}$$

where $S_d$ is the area of the surface $a'b'c'd'$.

Based on the above analysis, in the first vibration period, horizontal velocity can be given by

$$v_x = \begin{cases} -\dfrac{\pi f_1 A\cos(2\pi f_1 t)}{H + A\sin(2\pi f_1 t)}x & 0 \le t < \dfrac{1}{2f_1} \\ -\dfrac{\pi f_1 A\cos(2\pi f_1 t)}{H - A\sin(2\pi f_1 t)}x & \dfrac{1}{2f_1} \le t \le \dfrac{1}{f_1} \end{cases} \tag{27}$$

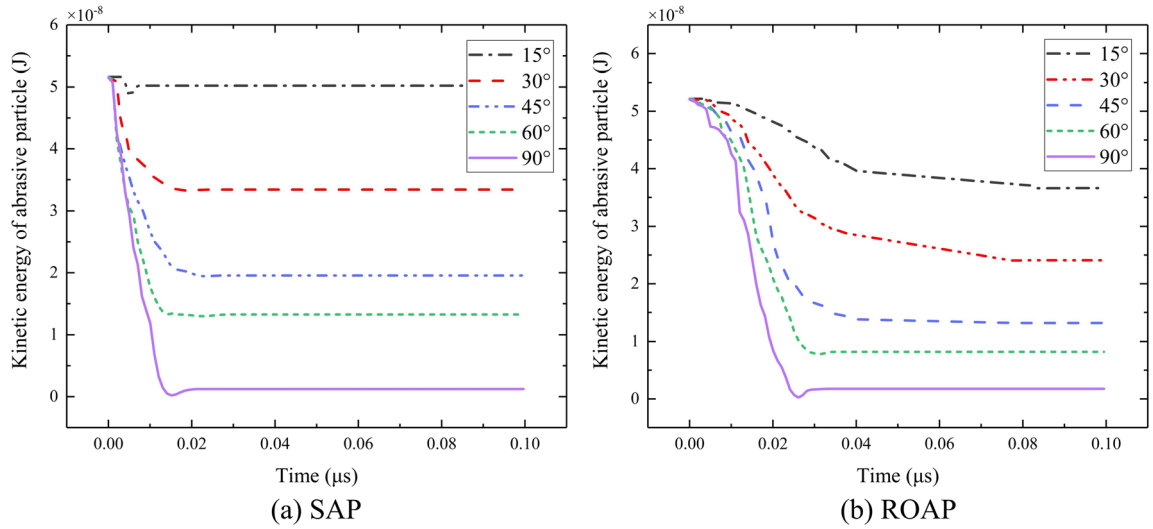


**Fig. 23** Time curves of kinetic energy loss with different impact angles: **a** SAP and **b** ROAP

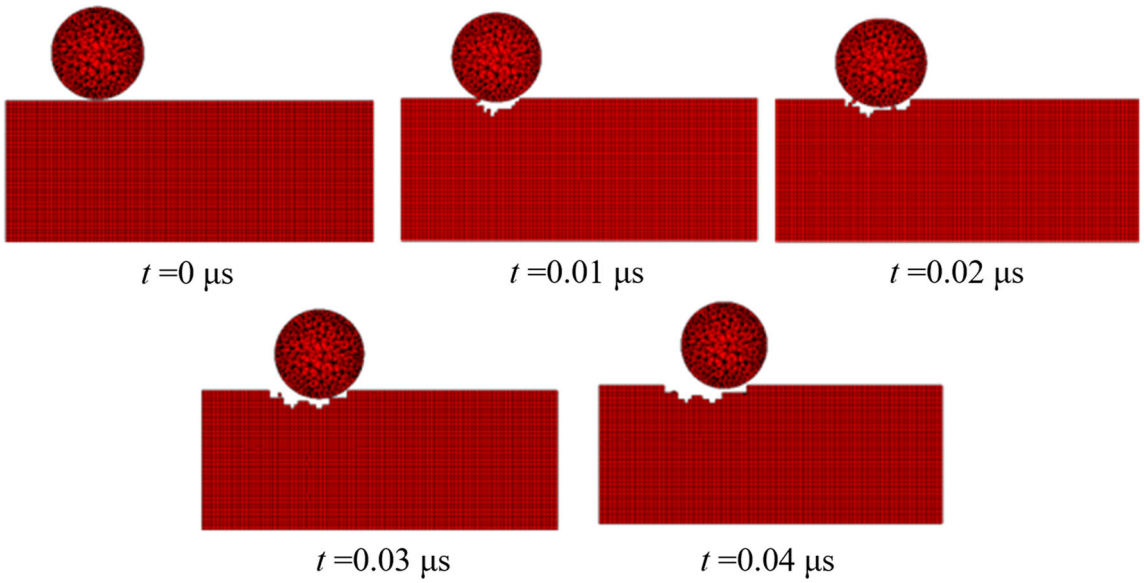


**Fig. 24** Impact process of SAP

Therefore, during the entire polishing process, the velocity in horizontal direction is as indicated above and changes periodically. The schematic of abrasive particles impacting the target material surface horizontally can be described as shown in Fig. 19.

When abrasive particles impact target material surface horizontally, the angle $\theta$ between velocity direction and tangent plane at the impact location on target material is defined as impact angle. According to the USP experiment results in the opening paragraph (in the first 20 min, surface roughness decreased sharply, then tended to be stable gradually) and the schematic shown in Fig. 19, at the initial stage of polishing, the surface of the target material is rough so that the impact angle is generally large; the surface roughness therefore decreased rapidly in the first 20 min. As polishing time increases, the hillocks on target material surface will be gradually removed by abrasive particles; meanwhile, the impact angle also decreases gradually; therefore, when the polishing time approaches 50 min, surface roughness tends to be stable. Ideally, with the impact of abrasive particles, impact angle will gradually tend to 0°, and there is no material removal anymore. Finally, a high surface quality will be obtained. Therefore, the material removal mechanism is consistent with the USP experiments results.

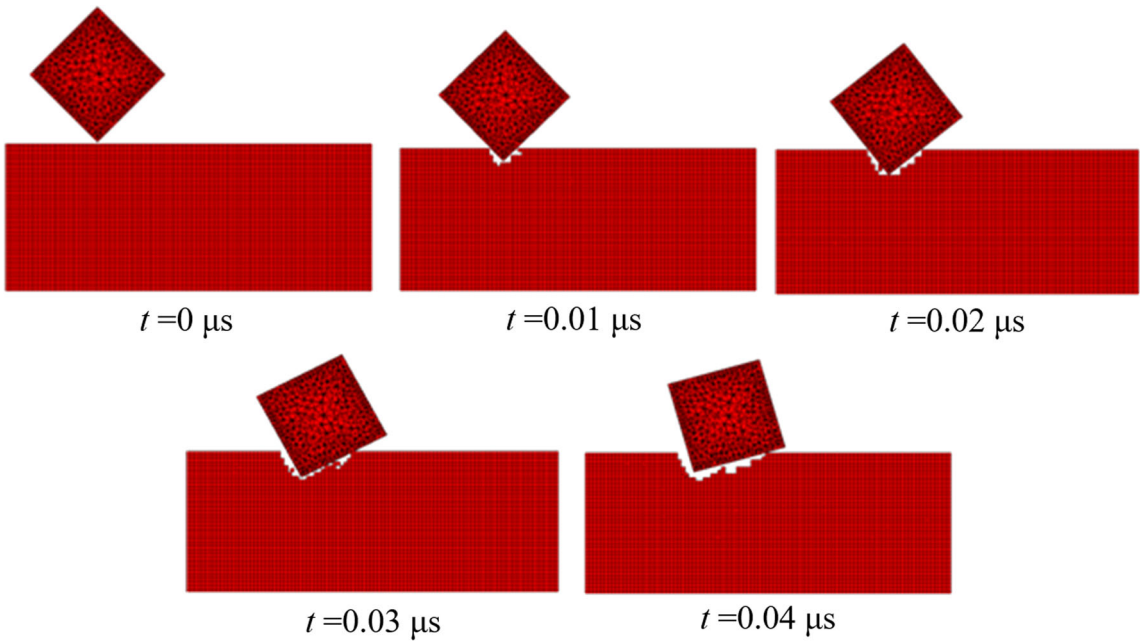


**Fig. 25** Impact process of ROAP

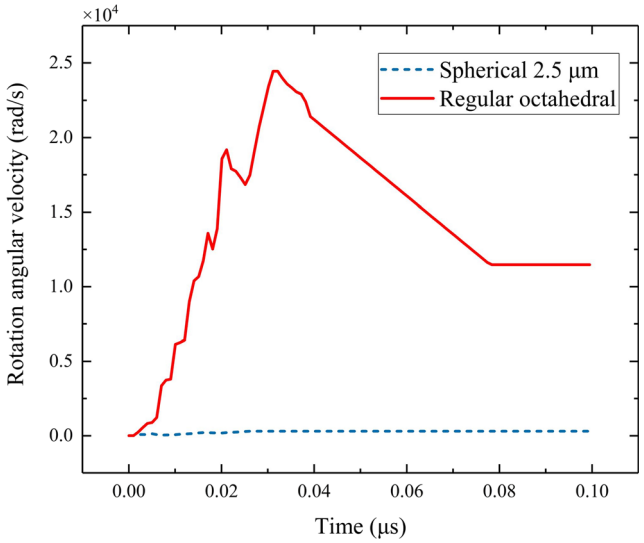


**Fig. 26** Time curves of rotation angular velocity of abrasive particles

#### 5.2.2 Finite element simulation of abrasive particle impact

According to the analysis of material removal mechanism and combining the method of Lv et al. [39], abrasive particle impacting monocrystalline silicon is simulated based on explicit dynamics LS-DYNA.

The selected abrasive particle material is diamond. Its performance parameters are listed in Table 3. Because of the high hardness of diamond, it is difficult to be crushed during an impact. Therefore, diamond abrasive particle is assumed to be rigid body in the simulation model.

Monocrystalline silicon was selected as target material. The Johnson-Holmquist ceramics (JH-2) was set as the material model, because JH-2 is suitable for describing the constitutive relation of hard and brittle materials under high strain rate conditions [40]. The parameters of the JH-2 model corresponding to monocrystalline silicon are shown in Table 4.

#### 5.2.3 Simulation procedure

Simulation procedure mainly includes (i) generating models based on CAD software, (ii) numerical simulation area dispersing based on HyperMesh, (iii) numerical simulation based on LS-DYNA, and (iv) numerical extraction and analysis based on LS-PrePost.

In order to analyze the effects of abrasive particle impact on target material surface, only the main factors such as impact force, impact time, energy loss, and MRR are stressed out while some unimportant factors are ignored. Therefore, the simulation model needed to be simplified and assumptions are made as follows

- Diamond abrasive particle is considered a rigid body. Its deformation and fracture are ignored during the impact process.
- Because monocrystalline silicon has anisotropy, its characteristic values of different directions are different. The characteristic values are considered identical; the stable direction <111> is studied [41, 42].
- The gravity is ignored during impact process.
- The impact time (0.01–0.05 μs), which is obtained from simulation results, compared with ultrasonic vibration period (50 μs), is extremely short and the velocity of STF flow field hardly changes in such an extremely short time. Therefore, during one impact, abrasive particle impacts the target material surface at a constant velocity.

As target material, a rectangular workpiece (10 μm × 7 μm × 4 μm) model is built. In order to simulate abrasive particles with blunt surface profile and with sharp surface profile, SAP and ROAP models are built. The volume of ROAP model is the same as that of SAP with a diameter of 2.5 μm. The diameters of SAP are set to 1.5 μm, 2.5 μm, and 3.5 μm. Impact velocities of abrasive particle are set to 30 m/s, 60 m/s, and 90 m/s. Impact angles are set to 15°, 30°, 45°, 60°, and 90°. Simulation model after meshing is shown in Fig. 20.

#### 5.2.4 Simulation results analysis

After calculation, the number of elements deleted from the model due to failure is counted and MRR is calculated. The MRR used to characterize the impact performance of the

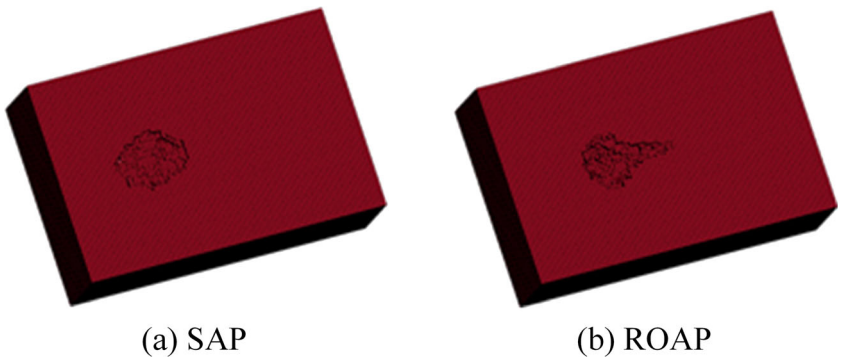


**Fig. 27** Target surface morphologies after impact: **a** SAP and **b** ROAP

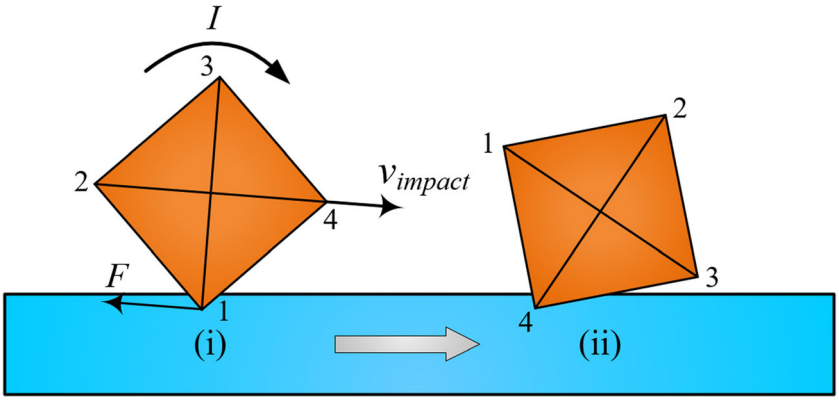


**Fig. 28** Force analysis of ROAP

target material is defined as the quotient of deleted workpiece elements mass and impact particles mass.

**Deformation analysis** SAP with diameter of 1.5 μm is used to analyze deformation. The impact angle is 30°. The impact velocities are 30 m/s, 60 m/s, and 90 m/s. The obtained relation time curve of model volume is shown in Fig. 21.

It can be seen that when impact velocity is 30 m/s, only a minimal elastic deformation occurs on the target surface. As the SAP rebound, the generated elastic deformation restores immediately. There is no essential effect on the target surface. When impact velocity increases to 60 m/s, elastic deformation occurs at the initial stage, then partially gradually restored. The total volume has a very small change, but there is no material removal, and plastic deformation occurs. When impact velocity is 90 m/s, there is obvious brittle material removal. Furthermore, compared with brittle removal, the effects of elastic deformation and plastic deformation on the workpiece model are negligible. Material removal mainly depends on brittle removal, only when impact velocity increases to a certain value which makes plastic deformation transition to brittle removal, the polishing efficiency will be improved.

**Effect of abrasive particle size and impact velocity on MRR** SAPs with diameters of 1.5 μm, 2.5 μm, and 3.5 μm are simulated. The impact velocities are 30 m/s, 60 m/s, and 90 m/s; the impact angle is 30°. The obtained relation curves between MRR and impact velocity are shown in Fig. 22.

Figure 22 shows that MRR increases with the increase of SAP size and impact velocity. Moreover, the difference between the SAP with different diameters also increases with the increase of velocity which means under the same USP condition, SAP with a large diameter and increasing impact velocity have a positive effect on the improvement of polishing efficiency. In STF of USP, the transverse shear flow changing from positive to negative makes the velocity of abrasive particle increase sharply. Therefore, the polishing efficiency is improved.

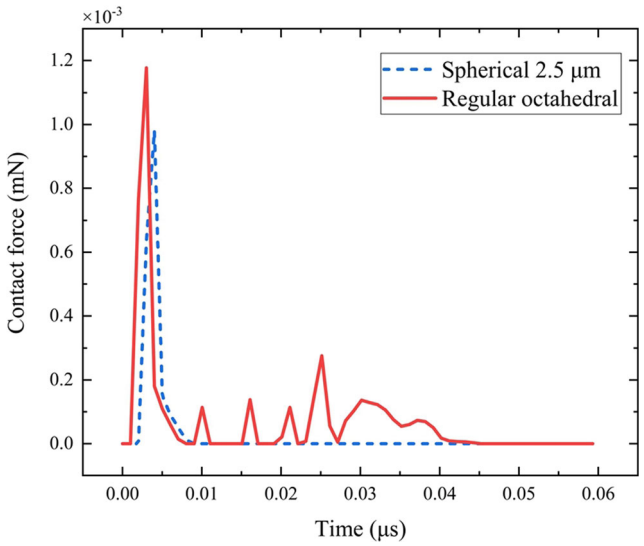


**Fig. 29** Time curves of contact forces

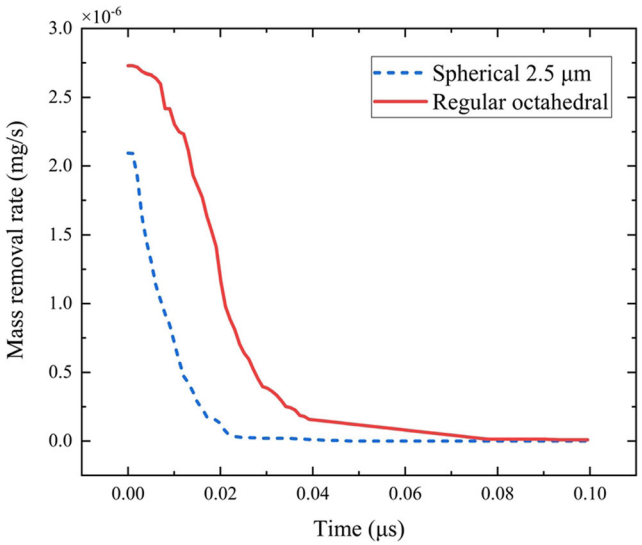


**Fig. 30** Time curves of mass removal rate

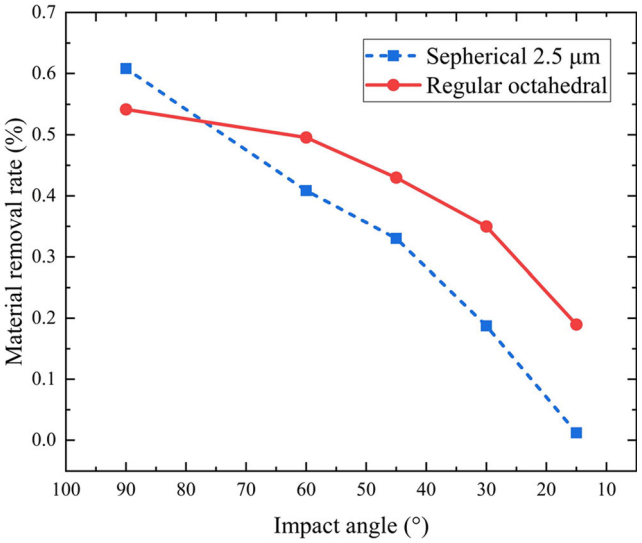


**Fig. 31** Relation curves of MRR and impact angle

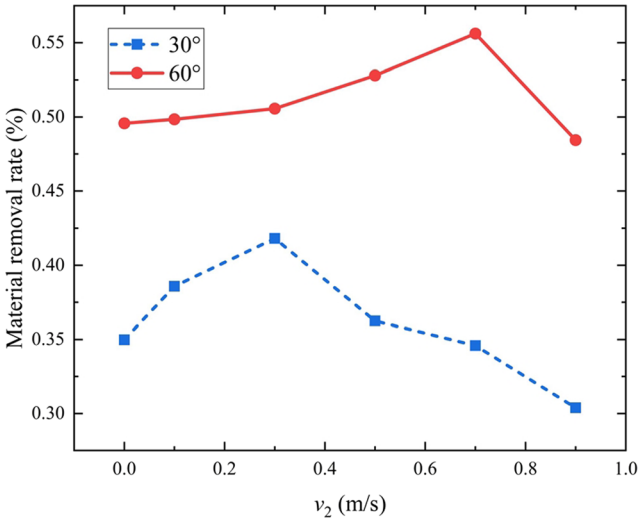


**Fig. 33** MRR curves of the impact angles of 30° and 60° with different $v_2$ values

**Kinetic energy change of abrasive particle during impact**

During impact, the kinetic energy loss of abrasive particles is mainly used for material removal. SAP with a diameter of 2.5 μm and ROAP of the same volume are simulated at the same velocity of 60 m/s with different impact angles of 15°, 30°, 45°, 60°, and 90°. The obtained time curves of kinetic energy loss are shown in Fig. 23.

Figure 23 shows that both the kinetic energy losses of SAP and ROAP increase as impact angle increases. The kinetic energy losses both are largest when impact angle is 90° and the final kinetic energy is almost zero which proves that nearly all of the kinetic energy is converted to the removal of material. The difference between SAP and ROAP is when the abrasive particles impact the workpiece model with a small angle, the kinetic energy loss of ROAP is relatively greater than that of SAP. In addition, by comparing Fig. 23 a and b, it is found that the kinetic energy loss of ROAP lasts about 0.027–0.04 μs while that of SAP is less than 0.015 μs. The kinetic energy loss of ROAP is larger because it has a longer interaction time with a workpiece surface which makes the conversion of energy more sufficient.

The simulated impact processes are shown in Figs. 24 and 25. The impact angle is 45°. According to Fig. 24, the rotation of SAP is invisible while that of ROAP is obvious in Fig. 25. The rotation angular velocities during the impact process are monitored as shown in Fig. 26 and the target surface morphologies after impact are shown in Fig. 27.

The ROAP produces an angular velocity during impact, whereas the SAP hardly rotates during impact. The force analysis of ROAP is shown in Fig. 28. When ROAP impacts the surface at a velocity $v$ (see Fig. 28 (i)), it is subject to the reactive force $F$ by target surface and thus obtains a torque $I$, which makes it continue to impact the target surface (see Fig. 28 (ii)). This continuous rotation process increases the interaction time between ROAP and target surface; therefore, more kinetic energy can be converted into the removal of material.

**Force analysis of the workpiece model during impact**

Simulation results of the average contact force between

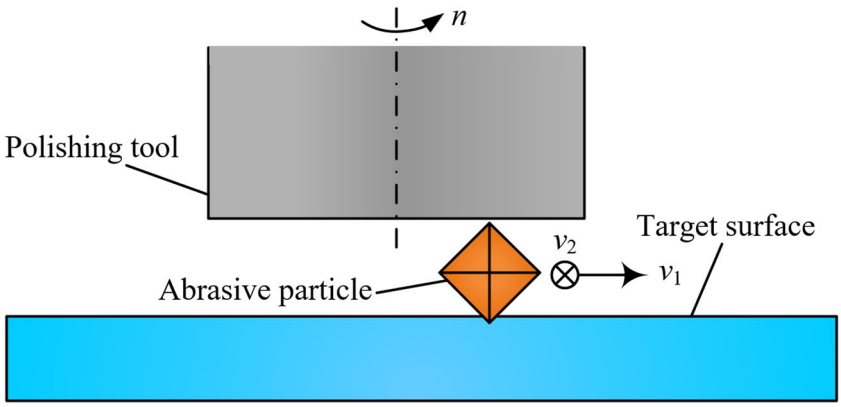


**Fig. 32** Schematic of USP when rotation is applied

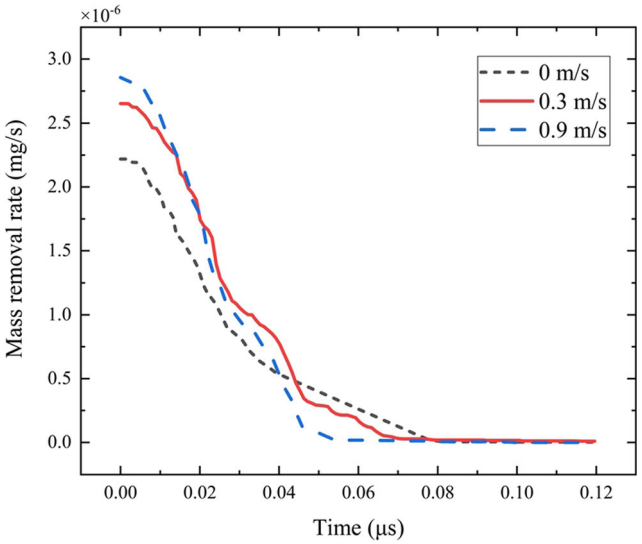


**Fig. 34** Mass removal rate curves (30°)

abrasive particles and workpieces are shown in Fig. 29. Within contact time, both contact forces of SAP and ROAP increase rapidly from zero initially, then gradually back to zero finally. And at the same impact angle and velocity, ROAP has firstly subjected a larger contact force at the moment of contact, then the contact force fluctuates continuously and decreases to zero finally, while SAP is firstly subjected to a maximal contact force, then immediately drops to zero.

When impact angle is 45° and impact velocity is 60 m/s, the time curves of mass removal rate are shown in Fig. 30.

When ROAP impacts target material surface, the stress is more concentrated than that of SAP because of its sharp profile. Therefore, the instantaneous contact force is greater compared with SAP, and ROAP has more material removal mass at the initial moment. Combined with Fig. 25, the rotation of ROAP results in an increase of contact time and more kinetic energy is used to remove material. Therefore, the material removal mass of ROAP is greater.

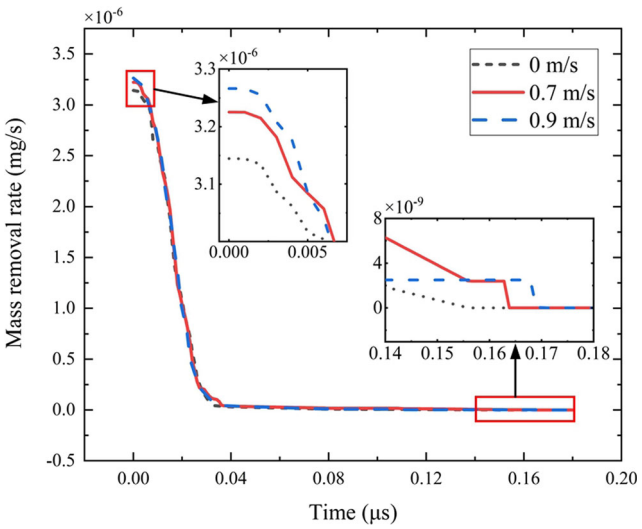


**Fig. 35** Mass removal rate curves (60°)

**Effect of impact angle on polishing efficiency.** When abrasive particles impact the target surface at a velocity of 60 m/s, the relation curves of MRR and impact angle are shown in Fig. 31.

It can be seen that when SAP and ROAP impact target surface at a certain velocity, they show the same trend. The material removal decreases with the decrease of impact angle, and it has a limit value when the impact angle is 90°. Overall, the MRR of ROAP is better than that of SAP except when the impact angle is close to 90°. That is because when the impact angle is small, ROAP has a strong rotation capability; therefore, the contact time is extended and material removal capability is improved as analyzed above. However, as impact angle increases, this rotation ability is attenuated; material removal capability decreases gradually.

The trend shown in Fig. 31 also explains at the initial stage of USP target surface is relatively rough; the impact angle is generally large (see Fig. 19); therefore, the polishing efficiency is high. As the abrasive particles impact constantly, target surface gradually becomes smooth; the impact angle decreases gradually therefore the polishing efficiency is gradually reduced.

### 5.2.5 Effect of polishing tool rotation on USP

According to the above analysis, abrasive particle size, abrasive particle profile, impact velocity, and impact angle all have great effects on the MRR of the workpiece model; however, the essence of the effects is the change of abrasive particles kinetic energy; that is how much kinetic energy is converted into the energy of material removal.

Therefore, in order to extend the contact time and improve kinetic energy conversion rate during the impact process, the rotation is applied to the polishing tool. The schematic is shown in Fig. 32; $v_1$ is the velocity of transverse shear flow caused by ultrasonic vibration; $v_2$ is the velocity increment caused by the rotation of the polishing tool.

Assume that the velocity caused by rotation equals to the linear velocity of the polishing tool at the position of the abrasive particle itself, which can be described as

$$v_l = \omega_s \times r = 2\pi n \times r \tag{28}$$

where $\omega_s$ is the angular velocity, $n$ is the spindle velocity, and $r$ is the distance of the abrasive particle from the rotation center.

In USP experiments, the diameter of the adopted polishing tool is 28 mm; the spindle velocities are 360 r/min, 480 r/min, and 600 r/min. The corresponding maximum velocities respectively are 0.528 m/s, 0.703 m/s, and 0.879 m/s. According to formula (14), the final velocity increment is

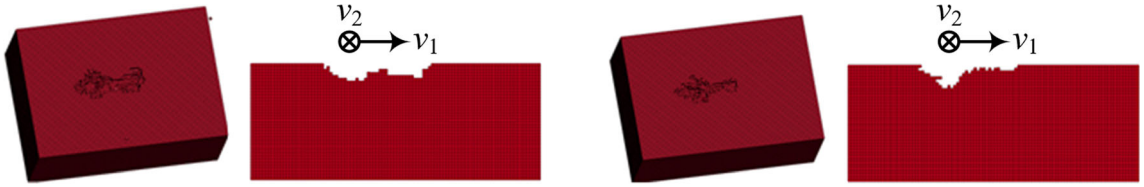


(a) 0.3 m/s (b) 0.9 m/s

**Fig. 36** Simulated surface morphologies (30°): **a** 0.3 m/s and **b** 0.9 m/s

$$v_2 = v_l e^{-\lambda \cdot l} \tag{29}$$

According to the formula (29) and experiments parameters, the velocity increment of abrasive particle has a maximum value of 0.9 m/s. Therefore, the velocity increments $v_2$ are set to 0.1 m/s, 0.3 m/s, 0.5 m/s, 0.7 m/s, and 0.9 m/s in simulation to verify its effect on MRR. ROAP is adopted, impact velocity is set to 60 m/s; and impact angles are 30° (fine polishing) and 60° (rough polishing).

**The effect of polishing tool rotation on MRR** Figure 33 shows MRR curves when impact angles are 30° and 60°, and $v_2$ are 0.1 m/s, 0.3 m/s, 0.5 m/s, 0.7 m/s, and 0.9 m/s.

As the $v_2$ increases, the variation trend of the two MRR curves both increase initially and decrease afterwards. The main difference is the variation trend of 60° MRR curve is relatively slow and its MRR reaches a maximum value when the $v_2$ is 0.7 m/s while the variation trend of 30° MRR curve tends to fluctuate a lot and its MRR starts to decrease when the $v_2$ is 0.3 m/s. Therefore, the conclusion can be drawn that at rough polishing stage, the increase of $v_2$ has a positive effect on MRR; however, at the fine polishing stage, the increase of $v_2$ does not necessarily improve polishing efficiency.

**Effect of polishing tool rotation on mass removal rate** According to Fig. 33, when impact angle is 30°, $v_2$ values are 0.3 m/s and 0.9 m/s; MRR reaches a maximum and a minimum value respectively; when impact angle is 60°, $v_2$ values are 0.7 m/s and 0.9 m/s; MRR reaches a maximum and a minimum value respectively. Therefore, in simulation, impact angles are set to 30° and 60° respectively; the corresponding velocity increment $v_2$ values are set to 0 m/s, 0.3 m/s, and 0.9 m/s and to 0 m/s, 0.7 m/s, and 0.9 m/s respectively. The simulation results are shown in Fig. 34 and Fig. 35.

As shown in Figs. 34 and 35, as $v_2$ increases, the higher the velocity, and the higher the corresponding mass removal at the beginning, but the duration of mass removal is relatively short. When impact angle is 30°, the mass removal rate curves of 0 m/s, 0.3 m/s, and 0.9 m/s have a big difference while that of impact angle 60° is small.

Combining Figs. 33, 34, and 35, the increase of spindle velocity overall has a positive effect on polishing efficiency. Once the target surface becomes smooth, the polishing efficiency is greatly affected by the spindle velocity, and excessive velocity will make the polishing efficiency decreased. Therefore, it is meaningful to increase the rotation velocity of the polishing tool within a certain range.

**Effect of an abrasive particle on the workpiece surface when applying spindle velocity** As can be seen from Fig. 36, compared with $v_2$ of 0.9 m/s, the material removal of 0.3 m/s is smoother; the impact depth is shallower; the impact scratch length is longer. It can be known that in fine polishing, $v_2$ of 0.3 m/s is conducive to the formation of the flat surface by comparing the material removal. However, in Fig. 37, the difference of $v_2$ does not result in a significant difference between morphologies of SAP and ROAP models and they have the same impact depth; the impact scratch length difference is less than 4%.

Based on the above study, at the initial stage of USP (e.g., the impact angle is 60°), the MRR increases with the increase of $v_2$ and there is no significant difference on the simulation topographies when $v_2$ changes. Thus, the increase of spindle velocity is meaningful to rough polishing stage. When in fine polishing stage (e.g., the impact angle is 30°), as $v_2$ increases, the overall material removal rate shows a trend of first increasing and then decreasing, and there is significantly difference on simulation topographies when $v_2$ changes. When $v_2$ is

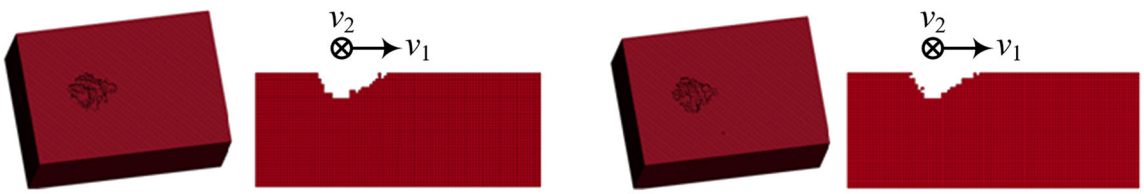


(a) 0.3 m/s (b) 0.9 m/s

**Fig. 37** Simulated surface morphologies (60°): **a** 0.3 m/s and **b** 0.9 m/s

0.3 m/s, MRR reaches the maximum. As shown by the simulation topography, the removal form of the material is also beneficial to the fine polishing. Eventually, however, the MRR starts to decrease, and the generated surface topography is not conducive to obtain a high-quality surface. Therefore, at the fine polishing stage, the increase of spindle velocity does not necessarily improve the polishing effect.

## 6 Conclusions

The interaction behavior of the material, STF flow field, and abrasive particle; the behavior of abrasive particles impacting monocrystalline silicon in STF flow field; and the effects of ultrasonic vibration on polishing quality are studied through experiments and simulations under USP in this paper. It is shown that ultrasonic vibration of the polishing tool has great influence on the mentioned above and conclusions can be summarized as follows:

(1) Monocrystalline silicon experimental results indicate the introduction of ultrasonic vibration to STF polishing has improved the polishing efficiency; meanwhile, the generated surface is also obviously superior to that of general polishing, increasing ultrasonic amplitude appropriately is beneficial and small size particles result in a better surface quality but a low polishing efficiency. As spindle velocity increases, the improvement of polishing efficiency belongs to the trend of first increase and then decrease. In initial stage of polishing, surface roughness decreases obvious, when polishing reaches a certain time; there is no significant difference in surface roughness.

(2) CFD simulations show that the internal pressure and velocity in STF flow field change periodically in USP. The flow field velocity in $x$ direction increases greatly while that in $z$ direction is relatively low, which indicates strong transverse shear flow is formed in STF. Moreover, its velocity and pressure increase with the increase of ultrasonic amplitude and the decrease of STF thickness. Under such conditions, the STF flow field in USP has provided a superior condition for an abrasive particle. The irregularity degree of abrasive particles impacting target material and impact velocity therefore has been increased as ultrasonic amplitude increases, which are contributions to improving polishing efficiency. This conclusion is consistent with the experimental results.

(3) Based on the characteristic of STF flow field in USP, a novel mathematical model of plastic deformation and brittleness removal when abrasive particles impact monocrystalline silicon is proposed in this study. No matter the material removal method is plastic deformation or brittle removal, the removal of material is affected by ultrasonic vibration frequency, ultrasonic amplitude, abrasive particle geometry, and material properties.

(4) Inspired by CFD simulation results that material removal mainly depends on transverse shear flow. Therefore, a novel material removal mechanism of STF of USP is proposed in this study, which reveals the immanent cause of the USP experimental results that, in the first 20 min, surface roughness decreases sharply, then tends to be stable gradually.

(5) The SAP (blunt) and ROAP (sharp) models are used to simulate abrasive particle impacting monocrystalline silicon with FEM; the results show that (i) MRR increases with the size of abrasive particle and impact velocity, (ii) more kinetic energy consumption of abrasive particle results in more material removal, and under the same conditions, the consumption of sharp abrasive particle is greater than that of blunt ones, because it produces a greater impact force and rotates during impact, and (iii) the effect of impact angle shows MRR decreases as impact angel decreases from 90° (first 20 min of USP, rough polishing) to 15° (approach to 60 min of USP, fine polishing) which is consistent with the experimental results and proves the conclusion of CFD simulation that material removal mainly depends on transverse shear flow.

(6) Effects of polishing tool rotation on USP show the increase of spindle velocity is meaningful to a rough polishing stage, and in fine polishing stage, the overall MRR shows a trend of first increasing and then decreasing as spindle velocity increases.

**Funding information** This work is supported by the Key Project of the National Nature Science Foundation of China (Grant No. U1508206), Science and Technology Planning Project of Shenyang (Grant No. 18006001), and Fundamental Research Funds for the Central Universities (Grant No. N160306006).

## References

1. Jain NK, Jain VK (2001) Modeling of material removal in mechanical type advanced machining processes: a state-of-art review. Int J Mach Tool Manu 41(11):1573–1635
2. Jain VK (2013) Advanced machining processes. In: Allied publishers private limited, New Delhi
3. Singh RP, Singhal S (2016) Rotary ultrasonic machining: a review. Advanced Manufacturing Processes 31(14):1795–1824
4. Fu R, Jia Z, Wang F, Jin Y, Sun D, Yang L, Cheng D (2018) Drill-exit temperature characteristics in drilling of UD and MD CFRP composites based on infrared thermography. Int J Mach Tools Manuf 135:24–37. https://doi.org/10.1016/j.ijmachtools.2018.08.002
5. Liang Z, Wang X, Wu Y, Xie L, Jiao L, Zhao W (2013) Experimental study on brittle–ductile transition in elliptical ultrasonic assisted grinding (EUAG) of monocrystal sapphire using single diamond abrasive grain. Int J Mach Tool Manu 71(8):41–51

6. Gong H, Fang FZ, Hu XT (2010) Kinematic view of tool life in rotary ultrasonic side milling of hard and brittle materials. Int J Mach Tool Manu 50(3):303–307
7. Kobayashi N, Wu Y, Nomura M, Sato T (2008) Precision treatment of silicon wafer edge utilizing ultrasonically assisted polishing technique. Journal of Materials Processing Tech 201(1):531–535
8. Jia D, Li C, Zhang Y, Yang M, Zhang X, Li R, Ji H (2019) Experimental evaluation of surface topographies of NMQL grinding ZrO2 ceramics combining multiangle ultrasonic vibration. Int J Adv Manuf Technol 100(1–4):457–473
9. Zhang D, Li C, Jia D, Wang S, Li R, Qi X (2014) Grinding model and material removal mechanism of medical nanometer zirconia ceramics. Recent Pat Nanotechnol 8:2–17
10. Yu T, Li H, Wang W (2015) Experimental investigation on grinding characteristics of optical glass BK7: with special emphasis on the effects of machining parameters. Int J Adv Manuf Technol 82(5-8): 1405–1419
11. Ralchenko VG, Ashkinazi EE, Zavedeev EV, Khomich AA, Bolshakov AP, Ryzhkov SG, Sovyk DN, Shershulin VA, Yurov VY, Rudnev VV (2016) High-rate ultrasonic polishing of polycrystalline diamond films. Diam Relat Mater 66:171–176
12. Hocheng H, Kuo KL (2002) Fundamental study of ultrasonic polishing of mold steel. Int J Mach Tool Manu 42(1):7–13
13. Suzuki H, Hamada S, Okino T, Kondo M, Yamagata Y, Higuchi T (2010) Ultraprecision finishing of micro-aspheric surface by ultrasonic two-axis vibration assisted polishing. CIRP Ann Manuf Technol 59(1):347–350
14. Chen F, Hao S, Miao X, Yin S, Huang S (2017) Numerical and experimental study on low-pressure abrasive flow polishing of rectangular microgroove. Powder Technol 327:215–222
15. Pereira FAR, Barrozo MAS, Ataíde CH (2007) CFD predictions of drilling fluid velocity and pressure profiles in laminar helical flow. Braz J Chem Eng 24(4):587–595
16. Ortiz-De-Zarate G, Madariaga A, Garay A, Azpitarte L, Sacristan I, Cuesta M, Arrazola PJ (2018) Experimental and FEM analysis of surface integrity when broaching Ti64. Procedia Cirp 71:466–471
17. Oezkaya E, Beer N, Biermann D (2016) Experimental studies and CFD simulation of the internal cooling conditions when drilling Inconel 718. Int J Mach Tool Manu 108:52–65
18. Mahnama M, Movahhedy MR (2010) Prediction of machining chatter based on FEM simulation of chip formation under dynamic conditions. Int J Mach Tool Manu 50(7):611–620
19. Lv Z, Huang C, Zhu H, Wang J, Hou R (2016) A 3D simulation of the fluid field at the jet impinging zone in ultrasonic-assisted abrasive waterjet polishing. Int J Adv Manuf Technol 87(9-12):1–13
20. Liu H, Wang J, Kelson N, Brown RJ (2004) A study of abrasive waterjet characteristics by CFD simulation. J Mater Process Technol 153-154(1):488–493
21. Woytowitz PJ, Richman RH (1999) Modeling of damage from multiple impacts by spherical particles. Wear s 233–235(99):120–133
22. Eltobgy MS, Ng E, Elbestawi MA (2005) Finite element modeling of erosive wear. Int J Mach Tool Manu 45(11):1337–1346
23. Yu T, Yang X, An J, Yu X, Zhao J (2018) Material removal mechanism of two-dimensional ultrasonic vibration assisted polishing Inconel718 nickel-based alloy. Int J Adv Manuf Technol (5–6):1–11
24. Yu T, An J, Yang X, Bian X, Zhao J (2018) The study of ultrasonic vibration assisted polishing optical glass lens with ultrasonic atomizing liquid. J Manuf Process 34:389–400. https://doi.org/10.1016/j.jmapro.2018.06.028
25. Paul S, Hoogstrate AM, Luttervelt CAV, Kals HJJ (1998) Analytical and experimental modelling of the abrasive water jet cutting of ductile materials. J Mater Process Technol 73(1–3): 189–199
26. Wang J, Shimada K, Mizutani M, Kuriyagawa T (2017) Effects of abrasive material and particle shape on machining performance in micro ultrasonic machining. Precis Eng 51:373–387
27. Shervanitabar MT, Mobadersany N (2013) Numerical study of the dielectric liquid around an electrical discharge generated vapor bubble in ultrasonic assisted EDM. Ultrasonics 53(5):943–955
28. Bifano TG (1991) Ductile-regime grinding : a new technology for machining brittle materials. Jtrsasmeserb 113(2):184–189
29. Tilly GP (1969) Erosion caused by airborne particles. Wear 14(1): 63–79
30. George J, Peter G (1985) Microindentation analysis of diammonium hydrogen citrate single crystals. J Mater Sci 20(9): 3150–3156
31. Lawn BR, Evans AG (1977) A model for crack initiation in elastic/plastic indentation fields. J Mater Sci 12(11):2195–2199
32. Sherif HA, Almufadi FA (2018) Analysis of elastic and plastic impact models. Wear 412-413:127–135. https://doi.org/10.1016/j.wear.2018.07.013
33. Rastegar V, Karimi A (2014) Surface and subsurface deformation of wear-resistant steels exposed to impact wear. J Mater Eng Perform 23(3):927–936
34. Huang C, Zhu H, Lu X, Li Q, Che C (2008) Transition mechanism from brittle fracture to ductile shear when machining brittle materials with an abrasive waterjet. Int J Precis Eng Manuf 9(2):11–17
35. Kumar N, Shukla M (2012) Finite element analysis of multi-particle impact on erosion in abrasive water jet machining of titanium alloy. J Comput Appl Math 236(18):4600–4610. https://doi.org/10.1016/j.cam.2012.04.022
36. Anwar S, Axinte DA, Becker AA (2013) Finite element modelling of overlapping abrasive waterjet milled footprints. Wear 303(1-2): 426–436
37. Liu ZG, Wan S, Nguyen VB, Zhang YW (2014) A numerical study on the effect of particle shape on the erosion of ductile materials. Wear 313(1-2):135–142
38. Zhu D, Yan S, Li B (2014) Single-grit modeling and simulation of crack initiation and propagation in SiC grinding using maximum undeformed chip thickness. Comput Mater Sci 92:13–21. https://doi.org/10.1016/j.commatsci.2014.05.019
39. Lv Z, Huang C, Zhu H, Wang J, Yao P, Liu Z (2015) FEM analysis on the abrasive erosion process in ultrasonic-assisted abrasive waterjet machining. Int J Adv Manuf Technol 78(9-12):1641–1649
40. Johnson GR, Holmquist TJ (1994) An improved computational constitutive model for brittle materials. Aip Conference 309:981–984
41. Gianchandani YB, Tabata O, Zappe H (2008) Editors-in-Chief. In: Gianchandani YB, Tabata O, Zappe H (eds) Comprehensive microsystems. Elsevier, Oxford, pp iii–iiv. https://doi.org/10.1016/B978-044452190-3.09002-9
42. Elwenspoek M (1993) On the mechanism of anisotropic etching of silicon. J Electrochem Soc 140(7):2075–2080